JGR Solid Earth

RESEARCH ARTICLE
10.1029/2022JB025729

Fault Weakening During Short Seismic Slip Pulse Experiments: The Role of Pressurized Water and Implications for Induced Earthquakes in the Groningen Gas Field

Jianye Chen[1,2], Luuk B. Hunfeld[2,3], André R. Niemeijer[2], and Christopher J. Spiers[2]

[1]State Key Laboratory of Earthquake Dynamics, Institute of Geology, China Earthquake Administration, Beijing, P.R. China, [2]Department of Earth Sciences, HPT Laboratory, Utrecht University, Utrecht, The Netherlands, [3]Now at The Netherlands Organization of Applied Scientific Research (TNO), Utrecht, The Netherlands

Key Points:

- Wet faults in Groningen gas field lithologies weaken significantly in a short seismic slip pulse while dry ones do not
- We observed fluid depressurization and dilation during seismic slip pulse, which is opposite to what is expected from thermal pressurization
- Small earthquake rupture experiences different resistance and slip weakening behaviors within different lithologies in the Groningen field

Supporting Information:

Supporting Information may be found in the online version of this article.

Correspondence to:

J. Chen,
j.chen3@uu.nl

Citation:

Chen, J., Hunfeld, L. B., Niemeijer, A. R., & Spiers, C. J. (2023). Fault weakening during short seismic slip pulse experiments: The role of pressurized water and implications for induced earthquakes in the Groningen gas field. *Journal of Geophysical Research: Solid Earth*, *128*, e2022JB025729. https://doi.org/10.1029/2022JB025729

Received 3 OCT 2022
Accepted 30 JAN 2023

Author Contributions:

Conceptualization: Jianye Chen
Data curation: Luuk B. Hunfeld
Funding acquisition: Christopher J. Spiers
Methodology: Jianye Chen, Luuk B. Hunfeld, André R. Niemeijer
Project Administration: Christopher J. Spiers
Supervision: André R. Niemeijer, Christopher J. Spiers
Writing – original draft: Jianye Chen

Abstract High-velocity friction experiments on simulated fault gouges sheared at high normal stress and to low displacement are particularly relevant to induced seismicity, which is becoming an important topic in fault mechanics. Using a new, improved set-up, which allows simulation of fault stress and fluid pressure (P) conditions approaching in-situ reservoir values, we performed ring-shear experiments on simulated fault gouges prepared from the source-, reservoir-, and caprock-formations of the Groningen gas field. Pre-sheared gouges were subjected to a rotational slip pulse reaching ~1.0 m/s peak velocity and 13–16 cm total displacement at effective normal stresses (σ_n^e) of 5–31 MPa and P up to 5 MPa, using water or dry nitrogen as pore fluid. All water-saturated gouges show strong dynamic weakening within a few cm of slip, with the lowest dynamic friction (0.2–0.4) measured at the highest σ_n^e. By contrast, the weakening was subtle in experiments using nitrogen. Our analyses focus on the high-P experiments, which are more realistic and show a distinct dependence of constitutive parameters (e.g., slip-weakening rate) on σ_n^e, in the form of empirical linear, power-law or exponential relations. The results provide much-needed constraints for numerical modeling of induced rupture propagation in the Groningen field. Based on temperature- and P-measurements made in near-direct contact with the active shear band, and using "post-mortem" microstructures, we exclude previously-proposed dynamic weakening mechanisms (e.g., flash heating or thermal pressurization) and suggest that water pressurization at heated asperity or grain contacts explains the weakening seen in our high-P experiments.

Plain Language Summary In the Groningen gas field of the Netherlands, induced seismic events have occurred since the 1990s. The strongest event occurred in 2012 with a magnitude of M_W 3.6. How faults slip during such small magnitude earthquakes (i.e., magnitude 3–4) is not clear, despite several recent studies. We conduct laboratory experiments to simulate the pulse-like (i.e., short but rapid) fault slip behavior characteristic for small magnitude human-induced seismicity, using a newly designed experimental set-up enabling monitoring of the slip behavior under stress and displacement closer to conditions relevant to faults in Groningen. We find that the different rock types present in the Groningen field offer various levels of resistance to rupture of small earthquakes, which is crucial information for modeling earthquakes and understanding seismic hazard and risk. In addition, based on observations of fluid pressure, temperature and dilatation during the experiments, we propose a fault weakening mechanism occurring on the micrometer scale, that can explain our observations.

1. Introduction

Fluid production from and injection into subsurface reservoirs can cause multiple (micro)seismic events near boreholes and in surrounding fracture networks, as well as causing creep or seismic slip events on pre-existing faults (Ellsworth, 2013). In the giant Groningen gas field (northeast Netherlands), induced seismic events have occurred since the 1990s, with the strongest occurring on 16 August 2012 with a magnitude of M_W 3.6. Most events are interpreted to occur along the pre-existing, high-angle, normal faults that crosscut the Slochteren sandstone reservoir and associated claystones, the overlying basal Zechstein caprock and the underlying Carboniferous siltstone/shale source rocks (Van Eijs et al., 2006). Assuming a circular slip patch, and using the statistical relation between rupture area and earthquake magnitude given by Hanks and Bakun (2008), the larger M_W 3–4 events correspond to rupture length-scales of 350–1,155 m, which do not necessarily rupture the entire fault length in the downdip or strike directions (Figure 1). From kinematic modeling of earthquake rupture processes in

Writing – review & editing: Luuk B. Hunfeld, André R. Niemeijer, Christopher J. Spiers

the Groningen fields, earthquake of these sizes may cause maximum shear displacement up to 0.1–0.2 m (Buijze, van den Bogert, et al., 2017; Wentinck, 2018). To assess the potential of fault reactivation to trigger larger earthquakes than observed to date, for example, by rupture propagation to depths below the reservoir where tectonic stresses may be present in the Carboniferous substrate, a thorough understanding of the mechanical properties of the fault rocks, is needed, especially under seismic slip conditions. Indeed, these data are crucial for constraining numerical modeling of fault rupture and associated seismic hazards (e.g., Buijze et al., 2019; Hergert et al., 2022; Richter et al., 2020; van Wees et al., 2017; Weng et al., 2021).

High-velocity friction (HVF) experiments on fault gouges, simulating major natural earthquakes, have been performed by numerous authors under conditions of relatively low (effective) normal stress (<10 MPa), large shear displacements (a few meters), and constant slip rates of 0.1–1.3 m/s (Boneh & Reches, 2018; De Paola et al., 2015; Di Toro et al., 2011). A dramatic drop in apparent friction coefficient (i.e., shear stress/applied effective normal stress) to values around 0.1 is always observed in such experiments, regardless of the lithology, and is interpreted to be related to temperature rise due to frictional heating (Di Toro et al., 2011; Rice, 2006). Because of the sealing difficulties, most previous HVF studies on water-saturated gouges report the frictional strength as the apparent friction coefficient, with poor knowledge of the pore pressures and thus the solid-to-solid friction (Kuo et al., 2021, 2022; Yao et al., 2018). To resolve the hydro-thermo-mechanical processes responsible for the observed weakening, recent efforts have been made to enable the monitoring of the thermal, dilatant and fluid drainage conditions of the simulated fault zones (Aretusini et al., 2021; Oohashi et al., 2015; Violay et al., 2014). It turns out that most studies suggested flash heating and thermal fluid pressurization to be the most efficient weakening mechanisms for a wet gouge-filled fault (e.g., Kuo et al., 2021; Ujiie et al., 2013), although other processes could also be important under ad hoc circumstances, such as vaporization and enhanced subcritical crack growth (Acosta et al., 2018; Chen et al., 2017; Rempe et al., 2020).

To simulate the source function of a natural earthquake, slip pulse experiments have been performed on bare rock surfaces or natural fault gouges at room-dry and low normal stress (<12 MPa) conditions (Liao et al., 2014—granite; Sone & Shimamoto, 2009). Over a few meters of displacement, the results showed a dramatic drop in friction coefficient from 0.7–0.8 to 0.2–0.3. However, these results cannot be directly applied to small-magnitude earthquakes, such as induced earthquakes in Groningen, where the fault slips in a short pulse over a few centimeters or decimeters (e.g., Wentinck, 2018). Hunfeld et al. (2021) performed rotary-shear experiments on simulated fault gouges collected from the main lithologies in the Groningen reservoir system under water-saturated conditions, imposing a short slip pulse at effective normal stresses up to 20 MPa with the initial pore water pressure at the circular sample margins being limited by leakage to atmospheric pressure ($P_i \sim 0.1$ MPa). Their results showed a modest but rapid weakening within 0.13–0.19 m of total displacement. Based on results from fluid pressure and temperature (P–T) sensors near the sample-piston interfaces and from numerical modeling, Hunfeld et al. interpreted thermal pressurization and vaporization of the pore fluid as a possible mechanism responsible for the observed dynamic weakening. However, the results were complicated by inconsistencies obtained using different sample assemblies (ring shear pistons or "forcing blocks" vs. solid cylinders), especially for clay-rich gouges such as the Carboniferous material, and by the effects of slip localization on P–T measurements made near the sample-piston interfaces. Moreover, no dry or gas-saturated control experiments were performed to isolate the effects of water. Recently, Aretusini et al. (2021) performed seismic slip experiments on clay-rich gouges using a novel set-up that allowed measurements of fluid pressure. The results showed that, during seismic slip over displacements of ∼0.4 m, shear-induced dilatation was followed by pressurization of the pore fluid, which, in combination with the low permeability of clay-rich fault gouge, may promote earthquake rupture propagation. Harbord et al. (2021) performed seismic slip experiments with a displacement of 1.65 m employing a realistic seismic source function compatible with source kinematics of large earthquakes (i.e., $M_W \geq 7.0$). In this case, friction evolved to show a strong dependence on the applied slip history, while parameters such as weakening distance scaled with the impulsiveness of the applied source function.

In the present study, we designed a new, better instrumented, and better confined and pressurized ring-shear set-up, enabling closer mimicking of stress and fluid conditions approaching in-situ reservoir values. For the first time, the new set-up also enabled monitoring of local fluid pressure and temperature (P–T) evolution in near-direct contact with the actively shearing slip surface or zone. We extended the conditions of the experiments reported by Hunfeld et al. (2021) to higher normal stress (up to 31 MPa) and used pressurized water as a pore fluid, both of which are closer to reservoir conditions at 3 km depth and have not been extensively explored before due to sealing difficulties at high speeds. We also performed new, dry control experiments using

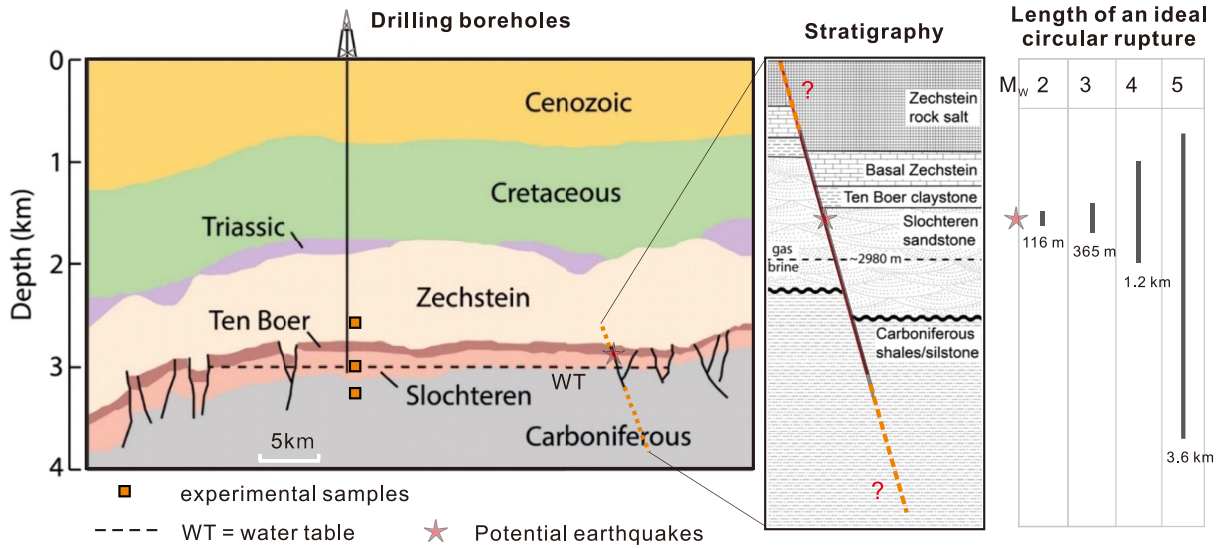

Figure 1. Schematics of the stratigraphy and fault systems in the Groningen gas field and potential induced earthquakes of various magnitudes. The rupture length is calculated using the statistical relation between rupture area (A) and earthquake magnitude ($M_w = \log A + 3.98$, where A in unit of km^2) given by Hanks and Bakun (2008), assuming circular ruptures.

pressurized N_2. The results show that the pressure P of pore water is essential in determining dynamic friction behavior. A systematic set of high-P experiments was further performed, providing new, improved data and advancing our understanding of the dynamic weakening process during a small earthquake (i.e., magnitude 3–4). The results are presented in a form suitable for use in numerical models, and the implications of our findings for induced seismicity in Groningen and other fields are discussed. Based on the microstructural observation and the P–T measurements made extremely close to the active slip surface, we also consider the possible microphysical processes causing weakening during a short seismic slip pulse in a fluid-pressurized fault. Specifically, our new observations allow us to eliminate almost all generally accepted dynamic weakening mechanisms such as thermal pressurization (Hunfeld et al., 2021) and result in a new hypothesis for dynamic weakening.

2. Samples and Experimental Methods

2.1. Samples

The gouge materials used were derived from the following Groningen lithologies (see Hunfeld et al., 2017), that is, from the Permian Basal Zechstein caprock, the underlying Slochteren sandstone reservoir, and the Carboniferous siltstone/shale substrate (Figure 1). Simulated fault gouges were produced by crushing drill core material or cuttings recovered from these units, that is, from the Stedum-1 and Zeerijp-2 boreholes located in the seismogenic central part of the Groningen field (provided courtesy of the Nederlandse Aardolie Maatschappij B.V., NAM). The crushed material was sieved to a particle size fraction of less than 150 μm (i.e., cf., 50 μm sieve size used by Hunfeld et al., 2017). X-ray diffraction analysis showed that the Basal Zechstein caprock gouge consists of anhydrite (48 wt%), carbonates (32 wt% calcite and dolomite), barite (14 wt%), and minor amounts (<10 wt%) of quartz. The Slochteren sandstone gouge contains quartz (67 wt%), feldspar (19 wt%), and minor amounts of carbonates and phyllosilicates (kaolinite and phengite). The Carboniferous shale gouge consists of quartz (55 wt%), phyllosilicates (35 wt% in total, with 21 wt% illite/chlorite and 14 wt% muscovite/phengite) plus feldspar (10 wt%) (see Hunfeld et al., 2017).

2.2. Experimental Set-Up

Friction experiments were performed on water- or N_2-saturated gouges at total normal stresses of 5–33 MPa, using the high-velocity rotary shear apparatus installed at the State Key Laboratory of Earthquake Dynamics in Beijing (Figure 2a). We employed a purpose-built annular ring-shear assembly (outer diameter = 40 mm, inner diameter = 28 mm), consisting of two pistons (forcing blocks) made of low thermal conductivity Ti-alloy, sandwiching an approximately 1 mm thick gouge layer (Figure 2b). The surface of the upper (rotating) piston

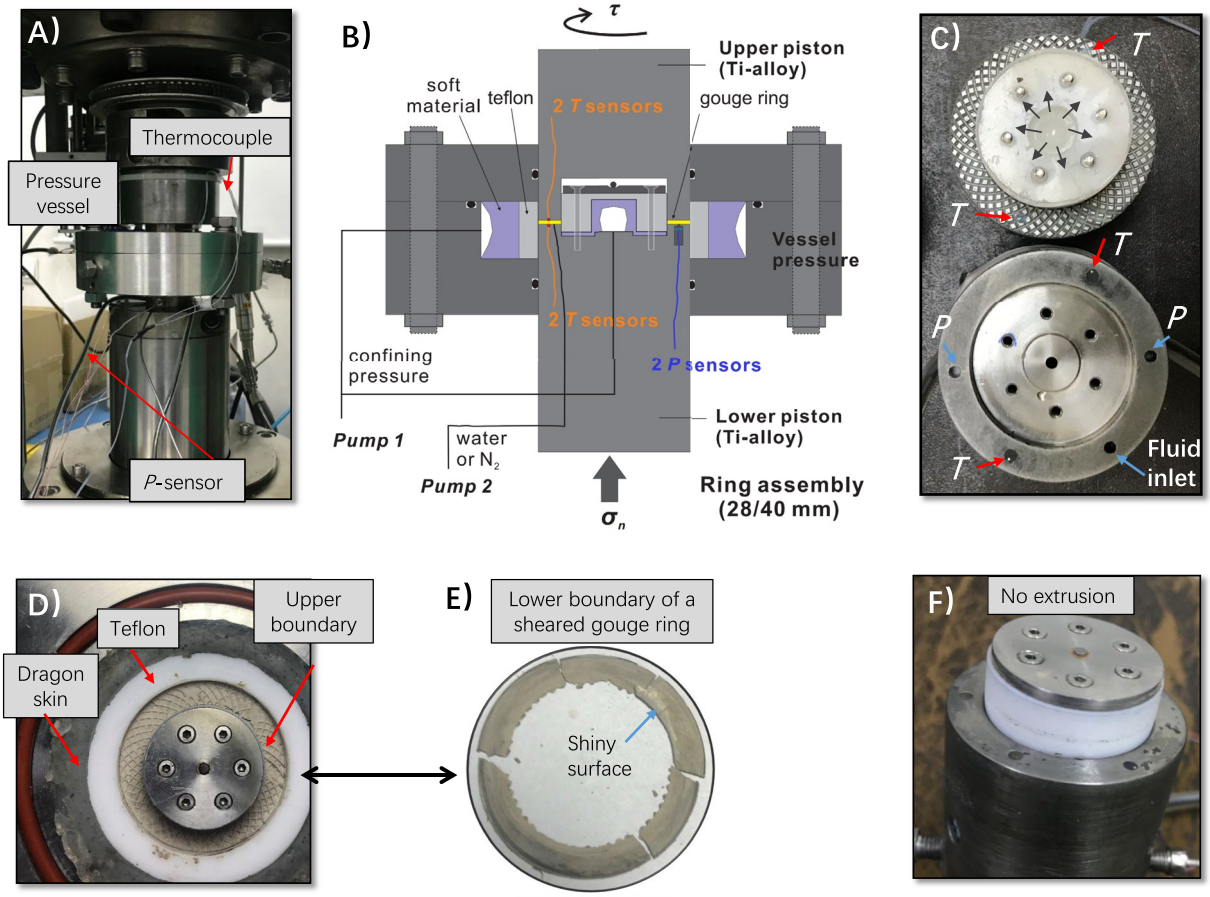

Figure 2. Experimental set-up. (a) Photograph of the pressure vessel used in the present study; (b) schematic diagram of the pressure vessel; (c, d, e), photographs of the upper and lower ring-shaped pistons and the post-experimental gouge layers, from both sides; and (f) photograph of the inner Teflon sealing ring. Note that four thermocouples (*T*) were located at the upper and lower sample-piston interfaces (two each). The lower piston accommodated two pressure (*P*) sensors placed in a 2 mm deep recess (from the gouge-piston interface).

was machined with grooves having a width of 0.5 mm, a depth of 0.25 mm, and a spacing of 1.0 mm (Figure 2c), while the surface of the lower (stationary) piston was ground with #80 SiC (180 μm). With these surface roughnesses, seismic slip tended to localize near the lower, *P*–*T* sensor-bearing boundary of the simulated gouge layer (Figures 2d and 2e). A tightly-fitting Teflon outer ring and inner cylindrical sealing block (hollow, internally pressurized plug) were used to confine the ring-shaped gouge layer (Figure 2b). To minimize gouge extrusion, especially under high axial normal stress, a pressure vessel connected to a syringe pump ("*Pump 1*") was used to apply a confining pressure of 2–5 MPa to the outer and inner Teflon ring and sealing block. The pressure vessel and the internal bore of the Teflon sealing block, were filled with a soft silicone mold (Ecoflex "Dragon Skin," see the blue areas in Figure 2b), acting as a gasket. This ensured an even distribution of pressure while preventing the confining fluid (water) from infiltrating the sample assembly. In almost all the experiments performed, this confinement approach successfully prevented both the fault gouge layer and the pore fluid from gaining access to the Teflon-piston interfaces (Figure 2f). In addition, lubricated Viton O-rings were used as static and dynamic pressure seals located between the pressure vessel and the lower and upper pistons, respectively.

To measure temperature (*T*) and pore fluid pressure (*P*) during the experiments, two pressure transducers (10 MPa full range, with 0.01 MPa resolution and less than 10 ms response time) and two Ni-Cr thermocouples (with a response time of 10–30 ms) were installed at different radial positions in the lower stationary piston (Figure 2b). Another two Ni-Cr thermocouples were installed on the upper (rotary) piston, using long compensation wires to allow the amount of upper-piston rotation needed for the experiment. The thermocouples were insulated in the pistons using corundum tubes, glued in place with high-temperature cement, with the active junctions located flush with the ground piston surfaces, that is, just in contact with the gouge layer. As verified by the previous

experiments reaching the buffered temperature of vaporized water (i.e., ~100°C), this technique can closely measure the bulk temperature of a shearing gouge in the HVF experiment (>10 m slip, Chen et al., 2017). The pressure transducers, which are 8 mm in diameter and 20 mm in length, were mounted 2 mm below the roughened sliding surface, filling the recess with 63 μm sieving mesh to prevent gouge intrusion whilst maintaining sufficiently-high permeability to allow pressure transmission. The void space around each transducer, including the 2 mm-diameter recess, is ~25 mm^3. To enable controlled fluid pressure to be imposed prior to each run, a second syringe pump (ISCO-D65) was connected to a pressure inlet located in the lower piston ("*Pump 2*," Figure 2b). As demonstrated by a calibration test, the pressure transducers can track fast changes in fluid pressure as imposed by the pump, at least up to ±5 MPa/s (Figure S1 in Supporting Information S1). As shown later, this is fast enough to capture most of the fluid pressure changes occurring at the active transducer tips during an experiment.

2.3. Experimental Procedure

In setting up each experiment, we first centered the upper rotary piston with respect to the loading frame axis within 2 μm, measured using a micrometer. The set-up was assembled by locating the confining vessel plus the Teflon seals (outer sleeve and inner cylindrical block) onto the lower piston. The gouge layer was then emplaced by distributing 1.2 g of gouge onto the roughened surface of the lower piston. The lower piston plus vessel assembly was subsequently moved upwards by advancing the pneumatic actuator so that the vessel slid over the upper piston until the latter was in contact with the gouge layer (i.e., until an axial normal stress, σ_n, of 0.3–0.5 MPa was established). The gouge layer was then evacuated via the pore fluid connections in the lower piston for ~10 min before being saturated with de-ionized water using *Pump 1* at 0.2–0.5 MPa or with N_2 using a gas regulator. Full saturation of the gouge layers was ensured by monitoring and achieving equal pore fluid pressure at the two pressure transducers installed in the lower piston, which usually took less than 10 min. After gouge saturation, a confining pressure (P_c) of 2–5 MPa was applied to the outer and inner Teflon seals using *Pump 1*. The target axial stress σ_n was then slowly applied, and pore fluid pressure was controlled to remain at a constant initial level (P_i), achieving the targeted initial effective normal stress $\sigma_n^e = \sigma_n - P_i$.

Before imposing a high-velocity slip pulse, each gouge sample was pre-sheared, for a total of 3.6 full rotations at a constant speed of 0.0119 revolutions/second. This is equivalent to a total displacement of 0.4 m at a constant equivalent slip velocity (V) of 1.5 mm/s (where V is defined at radius R of 17.18 mm, following Ma et al. (2014)). During the pre-shear, the gouge layer was connected to a controlled pump fluid pressure (i.e., *Pump 2*), but the drainage was not fast enough to keep the local pore pressure equal to the pump pressure. The pre-shear test is expected to accomplish comminution, compaction and shear band formation (Faulkner et al., 2018). Its purpose is to suppress the fluid pressurization effects due to shear-enhanced gouge compaction during the high-velocity slip pulse (Chen et al., 2017; Kuo et al., 2022; Rempe et al., 2020).

After pre-shear, the shear load was removed, and the local temperature and pore pressures measured were allowed to equilibrate to approach room temperature and P_i, respectively. Temperature equilibration took 1–3 min. Pressure equilibration typically took a few minutes in the case of Slochteren sandstone gouges, versus 30 min to a few hours in the case of Basal Zechstein and Carboniferous gouges. The equilibration time was reduced by a factor of 2–4 when N_2 was used as the fluid medium. Once stable, a high-velocity slip pulse was imposed under undrained conditions, that is, with closed-in pore fluid initially at pressure ~P_i. To generate this pulse, the motor control system was programmed through a function generator to apply an asymmetrical, triangular velocity profile characterized by a peak target speed of 11.9 revolutions per second and a total displacement of 1.19 revolutions. This is equivalent to 1.5 m/s peak velocity and 0.15 m total displacement occurring over ~0.25 s. With these settings, the output velocity profiles were not perfect sawtooth triangles but evolved continuously during the pulse, due to machine response characteristics, with a peak being reached at 0.14 ± 0.02 s. The actual peak velocity reached varied between 1.05–1.46 m/s and decreased with increasing σ_n^e. The same trends were seen in the output of total displacement, which decreased from 0.156 to 0.115 m with increasing σ_n^e. The peak velocity and total displacement values achieved were, therefore, less than the target values but reflect good system performance considering the challenges in achieving a controlled high-velocity, short-displacement slip pulse. In one experiment performed on the Carboniferous gouge, we doubled the input target displacement (2.38 revolutions), generating a total displacement of 0.272 m, while keeping the same peak velocity.

A total of 34 experiments were performed on the three simulated gouge materials considered, including 10 runs using gas N_2 as pore fluid medium. The N_2 experiments mainly focused on Slochteren sandstone, the principal

reservoir rock of the Groningen gas field. All the tests performed are listed in Table 1, along with the corresponding conditions and key observations.

2.4. Data Acquisition and Analyses

During the experiments, axial load, axial displacement, torque, upper piston rotation (hence angular speed), temperature, and pore fluid pressure signals were recorded at a rate of 10 Hz and 2 kHz for the pre-shear and pulse-shear stages, respectively. The raw data were processed to obtain equivalent slip velocity (V, m/s), equivalent shear stress (τ, MPa), normal stress (σ_n, MPa), fluid pressure (P, MPa), and apparent friction coefficient, defined $\mu_a = \tau/(\sigma_n - P_i)$, versus displacement ($d$) and time ($t$). Like equivalent slip velocity, translation of torque to equivalent shear stress followed the standard method (Ma et al., 2014). No correction for the small displacements related to machine/sample shear stiffness was applied in calculating shear displacement. The axial displacement data obtained are taken to represent changes in the gouge layer thickness directly, since machine expansion/contraction due to stress or temperature variations during the experiments is of much smaller order. To obtain μ_a versus displacement (d) curves during the seismic slip pulse, the 2 kHz friction data were smoothed using a moving average method with a window of 60 or 120 data points, and the displacement was calculated from the revolution rate and converted into equivalent displacement d measured at R of 17.18 mm (Ma et al., 2014).

Without sample extrusion, the shear resistance due to seal friction (i.e., from the Teflon-piston interfaces and the O-ring) was negligible compared with that offered by the gouge friction, under all normal stress conditions applied. To further quantify the contribution of seal friction to the total torque measured, wet calibration runs were conducted in which the sample assembly was sheared using our standard high-velocity slip pulse—but with no sample present and with no contact between the upper and lower pistons. The torque measured due to Teflon friction was more or less constant during slip, reaching less than 5% of the peak torque levels measured in gouge experiments conducted at σ_n^e of 5 MPa. However, since Teflon seal friction likely varies from run to run, due to differences in the axial alignment of the set-up, no seal friction correction was applied to the gouge friction versus displacement curves.

Pore pressure measurements showed strong spatial and temporal variations during the high-velocity slip pulse, precluding the determination of effective normal stress and true friction coefficient. However, during pre-shear at low slip rates, the instantaneous fluid pressures measured by the two transducers present in the lower ring at different radial positions were, in most cases, almost equal, pointing to nearly homogeneous pore pressure within the gouge sample. The corrected friction coefficient during the pre-shear was thus determined using the following equation: $\mu_{cor} = \tau/(\sigma_n - P_{ave})$, where P_{ave} is the instantaneous fluid pressure averaged from the two transducers.

To conduct microstructural analysis, sample fragments were retrieved after the experiment and dried in an oven at 55°C. Recovered samples were first impregnated using epoxy resin and then sectioned normal to the shear plane using a thread diamond saw. Sections were cut tangential to a centrally inscribed circle with a radius of ~17 mm. In this way, the central portion of the section was oriented parallel to the imposed shear direction. Microstructural images were taken from the Au-coated thin sections using a Zeiss (Rigma Surpa 55) scanning electron microscope (SEM), operated in backscatter electron and secondary electron modes with an acceleration voltage of 10–15 kV. To eliminate damage to the fragile sandstone gouge sections, the recovered fragments were used directly for the SEM analyses after coating.

3. Results

3.1. Representative Experimental Data

To illustrate the pre-shear stage of our wet experiments (i.e., 0.40 m of displacement at a constant velocity of 1.5 mm/s), the typical results from a run performed on a Slochteren sandstone gouge sample at 10 MPa axial normal stress are shown in Figure 3. As slip was initiated, axial displacement showed a gradual contraction to a near constant level (by ~0.25 mm) after about 100 s, which can be interpreted as a reduction in the gouge layer thickness (Figure 3a). Alongside this, the pore pressures measured by the two transducers in the sample assembly showed an abrupt increase by ~ 6 MPa, which then gradually decreased until reaching a steady level of 1.8 MPa after ~250 s as slip continued. The temperatures measured, using the four, near-sample thermocouples described above, showed a gradual increase by ~10°C during the imposed slip, but with large (~5°C–10°C) superimposed fluctuations (Figure 3b). An immediate decrease in measured temperature occurred as the motor stopped. The apparent friction coefficient versus time evolution showed a peak value of ~0.4 followed by a sharp decrease to

Table 1
Seismic Slip-Pulse Experiments and Key Information

Run	σ_n^e (MPa)	P_i (MPa)	ΔH_{dyn} (μm)	ΔH_{fin} (μm)	ΔP_{dyn} (MPa)	ΔP_{max} (MPa)	T_{max} (°C)	*Disp.* (m)	*Lc.*	P_c (MPa)	Remarks
Carboniferous shale											
2536	5.0	3.78	+9	−6	−1.2/+3.1	+3.4	42	0.16	L	4.0	
2428b	8.3	1.68	+10	+1	−0.5/+0.5	+1.2	98	0.15	L	5.0	
2498	9.4	4.52	−15	−20	−2.75/+0.68	+1.21	110	0.27	L	5.2	Low-σ_n preslip
2421	9.7	0.26	20	−8	−0.05/+0.08	+0.05	150	0.16	U	2.0	
2492	9.8	5.08	−20	−24	−0.68/+0.22	+0.86	110	0.16	L	5.0	Low-σ_n preslip
2545	10.8	3.10 (N_2)	+23	−80	−0.13/−0.05	+0.12	125	0.16	L	3.0	
2428a	14.6	5.25	−35	−40	−2.72/−1.46	+0.2	182	0.15	U	5.0	Low-σ_n preslip
2493	18.7	5.30	+16	−18	−1.0/+0.1	+1.40	213	0.14	L	6.6	
2537	20.7	3.13	+11	−4	−0.15/−0.21	+1.02	177	0.13	U	5.0	
2553a	27.4	1.29	−40	−90	−0.1/+0.02	+0.02	220	0.13	U	5.0	Low-σ_n preslip
2553b	31.4	1.28	−90	−130	−0.2/+0.03	+0.05	160	0.13	B	5.2	
1427	10	0.07	+33	+28	−0.03/−0.02	+0.05	44	0.15	U	2.0	Hunfeld et al. (2021)
1435	19.9	0.08	+34	+3	−0.07/+0.05	+0.29	137	0.15	U	2.0	Hunfeld et al. (2021)
1455	4.7	0.31	+29	+14	−0.02/+0.04	+0.03	41	0.15	U	2.0	Hunfeld et al. (2021)
Basal Zechstein											
2540	6.1	2.33	+41	−4	−1.94/−0.09	+0.19	78	0.16	L	4.0	
2417	9.8	0.20	+50	+8	−0.09/−0.06	+1.92	111	0.14	L	5.0	
2549	9.9	3.92	+2	−110	−0.12/−0.03	+0.05	138	0.16	L	4.0	
2550	10.7	3.11 (N_2)	+10	−50	−0.02/0.00	+0.15	142	0.15	L	4.5	
2496	11.1	2.80	+12	−12	−1.43/−1.00	+1.90	140	0.14	L	5.3	
2427	15.5	4.78	+20	−30	−2.36/−1.35	+2.37	161	0.13	L	5.0	
2497	19.0	5.11	+10	−25	−0.2/+0.1	+1.6	201	0.12	U	6.8	
2541	20.4	1.61	+13	−10	−0.11/−0.02	+0.16	153	0.12	L	5.0	
1436	10.0	0.31	+76	−24	−0.07/+0.05	+0.12	76	0.19	L	2.0	Hunfeld et al. (2021)
1442	20.0	0.63	+44	+2	−0.07/+0.15	+0.55	125	0.14	L	2.0	Hunfeld et al. (2021)
1456	5.0	0.41	+117	−10	−0.05/−0.03	+0.05	48	0.16	L	2.0	Hunfeld et al. (2021)
Slochteren sandstone											
2538	4.9	3.61	+16	+4	−1.45/−0.82	+0.14	108	0.16	L	4.0	
2423	8.3	1.68	+23	+2	−0.07/−0.02	+0.68	153	0.15	L	2.0	0.5 mm-thick gouge
2422	9.5	0.44	+20	−2	−0.15/+0.02	+0.21	117	0.14	L	2.0	
2494	9.6	4.41	+35	+7	−1.94/+5.01	+5.01	173	0.15	L	4.6	
2554	10.5	0.49	+14	−8	−0.04/+0.01	+0.05	154	0.14	U	2.2	
2495	20.1	3.85	+4	−20	−0.03/−0.06	+3.33	361	0.12	U	4.8	
2539	11.1	2.29	−11|+17	−6	−0.10/+0.03	+0.71	239	0.12	U	4.6	
1425	9.9	0.25	+18	+15	−0.02/+0.04	+0.58	52	0.15	U	2.0	Hunfeld et al. (2021)
1426	19.9	0.29	+12	−6	−0.05/+0.81	+1.41	65	0.13	U	2.0	Hunfeld et al. (2021)

Table 1
Continued

Run	σ_n^e (MPa)	P_i (MPa)	ΔH_{dyn} (μm)	ΔH_{fin} (μm)	ΔP_{dyn} (MPa)	ΔP_{max} (MPa)	T_{max} (°C)	*Disp.* (m)	*Lc.*	P_c (MPa)	Remarks
1457a	5.0	0.37	+12	+5	−0.03/+0.04	+0.13	39	0.16	U	2.0	Hunfeld et al. (2021)
1457b	5.0	0.46	+18	+9	−0.01/+0.03	+0.11	40	0.16	U	2.0	Hunfeld et al. (2021)
2546a	5.9	2.77 (N_2)	+21	−17	−0.01/−0.00	+0.12	166	0.16	U	3.0	
2551	10.7	3.08 (N_2)	+130	−110	−0.02/+0.01	+0.37	341	0.14	U	3.0	
2546b	16.3	2.72 (N_2)	+36	−51	−0.03/−0.02	+0.17	273	0.13	U	3.0	
2552c	20.7	2.25 (N_2)	+4	−53	−0.15/+0.02	+0.21	230	0.12	B	3.6	
2552d	21.0	0.21 (N_2)	−49	−60	−0.10/−0.05	+0.24	489	0.12	B	3.6	
2546c	21.8	2.70 (N_2)	+44	−34	−0.12/−0.04	+0.25	297	0.12	U	3.0	
2552b	26.6	2.04 (N_2)	−128	−134	−0.20/−0.10	+0.31	239	0.11	B	3.6	
2552a	26.9	1.78 (N_2)	−156	−186	−0.10/−0.04	+0.42	264	0.11	U	3.6	Low-σ_n preslip

Note. σ_n^e = nominal effective normal stress (applied normal stress σ_n minus P_i); P_i = mean value of initial fluid pressures measured at two transducer locations; ΔH_{dyn} = axial displacement change during slip acceleration (≤0.14 s, positive sign "+" for dilatation); ΔH_{fin} = final (net) thickness change during the seismic slip pulse, measured at the cessation of slip (~0.3 s); ΔP_{dyn} = immediate fluid pressure change during acceleration, where "/" separates measurement results from two transducers; ΔP_{max} = the maximum fluid pressure increase, usually achieved after the termination of the slip pulse (0.3 s–10 min); T_{max} = maximum temperature measured by the four thermocouples; *Disp.* = total shear displacement; *Lc.* = position of localized slip zone as indicated by the temperature measurements close to the upper and lower boundaries of the simulated gouge layer (~0.8 mm in thickness), where "U," "L," and "B" indicate localized slip in the upper, lower, and both boundaries, respectively; P_c = confining pressure exerted on the outer and inner Teflon walls to seal the gouge ring. Thermocouple and pressure transducer locations are shown in Figure 2. Pre-shear at 1.6 mm/s was conducted at the targeted σ_n^e, except in a few experiments the σ_n^e applied during pre-shear was lower than in the later seismic slip pulse (marked as "low-σ_n preslip").

0.2 within the first ~10 s of wet shear, and then by a gradual increase to a nearly steady level of 0.6 after ~80 s (Figure 3c). Assuming that the measured *P*-values reflect in-sample pore pressure, the corrected friction coefficient μ_{cor} showed a peak value of 0.95, quickly falling to a steady-state level of 0.75 within ~20 s of slip time.

Amongst all the pre-shear tests performed, the gouge prepared from Carboniferous siltstone/shale core material showed slightly more contraction with increasing effective normal stress, with a total reduction in the gouge layer thickness of 0.35–0.4 mm at 20 MPa effective normal stress. By contrast, thickness reduction during pre-shear in Slochteren and Basal Zechstein gouges was relatively smaller (<0.3 mm) and insensitive to effective normal stress. We note in the first place that the thickness changes during the subsequent seismic slip pulse tests were much smaller (<0.1 mm), sometimes even showing a dilatation. The pre-shear compaction was inferred to mostly stem from the formation of shear bands, characterized by strong grain size reduction and slip localization (cf., Kuo et al., 2022; Rempe et al., 2020). As revealed later by the microstructural analysis, the larger contraction (i.e., in Carboniferous shale gouges) was indicative of more compact gouge layers.

Figure S2 in Supporting Information S1 compiles friction data from all pre-shear tests performed, plotting the evolution of the corrected friction coefficient with shear displacement. The corrected steady-state friction coefficient (μ_{cor}) obtained, except a few outliers, falls in the range 0.72–0.84 for the Basal Zechstein, 0.60–0.74 for Slochteren sandstone, and 0.47–0.55 for Carboniferous shale/siltstone. These results, obtained at a slip rate of 1.5 mm/s, are generally consistent with the results obtained under in-situ reservoir *P-T* conditions at low slip rates (0.1–10 μm/s), considered representative of earthquake nucleation (Hunfeld et al., 2017). This consistence suggests that during the low-velocity pre-shear test, the two pressures measured at the opposite positions of the lower piston can roughly reflect the average fluid pressure within the gouge layer (Figure 2c). Note that the two pore pressures were not always consistent, possibly reflecting a poor hydraulic connection between the transducer and the gouge layer. Moreover, the filters used in the sensors could be slightly more open or clogged in the different positions. As a result, fluid pressures might have been higher than those measured, leading to corrected friction values lower than those expected in a few experiments (Figure S2 in Supporting Information S1).

Representative results obtained in the high-velocity slip pulse stages of a wet experiment are shown in Figure 4 (from run 2427 performed on simulated Basal Zechstein gouge material at 20 MPa axial normal stress and 4.7 MPa initial fluid pressure). Figures 4a and 4b show the evolution of temperature and fluid pressure with experimental

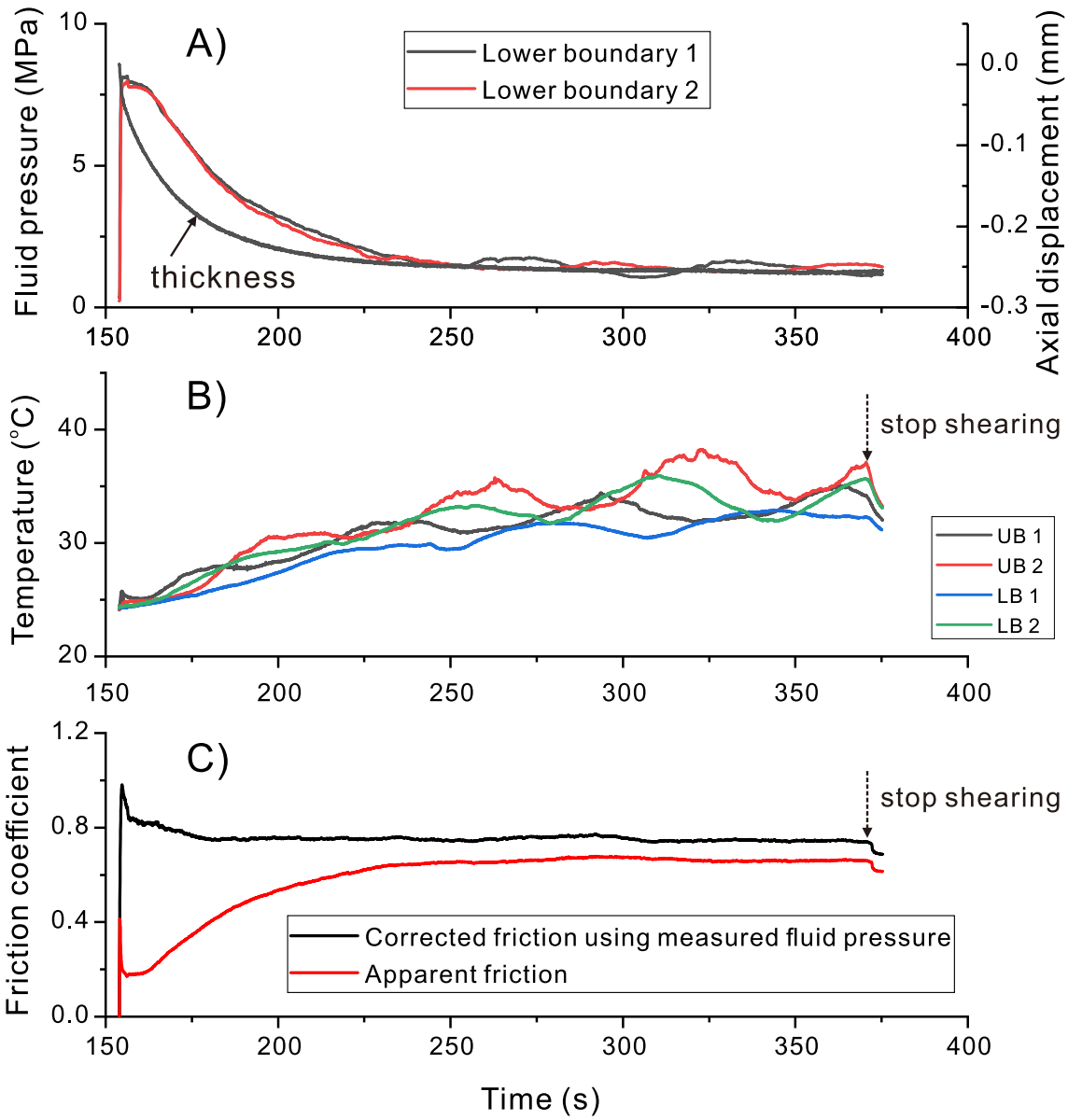

Figure 3. Results from the pre-shear stage of a typical experiment on simulated Slochteren sandstone fault gouge performed at a normal stress of 10 MPa and using a slip rate of 1.5 mm/s. (a) Fluid pressures measured at the lower sample boundary, plotted alongside measured axial displacement change; (b) temperatures measured at both boundaries of the gouge layer; (c) apparent friction coefficient, $\mu_a = \tau/(\sigma_n - P_i)$, and the corrected value, $\mu_{cor} = \tau/(\sigma_n - P_{ave})$, using the measured initial fluid pressure (P_i) and instantaneous average fluid pressure (P_{ave}) to obtain effective normal stress, respectively.

time. Figures 4c and 4d show the details of the results for the slip pulse, together with the changes occurring in axial displacement. During the slip pulse, which lasted ~0.25 s, temperatures measured at the lower boundary (LB) of the gouge layer were much higher than those measured at the upper boundary, with a maximum value of 161°C reached by the time slip ceased (Figure 4d). The LB temperature immediately decreased while the upper boundary temperature continued to increase for ~0.2 s, indicating that the imposed sliding was mostly accommodated close to the LB of the gouge layer. This interpretation is broadly consistent with the (micro-)structure of the samples retrieved after the experiments (see Section 3.5). Finally, both temperature values converged and decreased to ambient background levels within 200 s (Figure 4b). Unlike the pre-shear stage, little change (10s vs. a few 100s of micrometers) was observed in the vertical displacement signal during the slip pulse. This showed a dilatation of 55 μm followed by contraction, leading to net compaction of 30 μm after the experiment (Figure 4c). The two pressures measured at the lower sample boundary showed a minor decrease upon initiation of the slip pulse, followed by sharp decreases of 1.2 and 2.2 MPa near the point of maximum dilatation, then recovering to

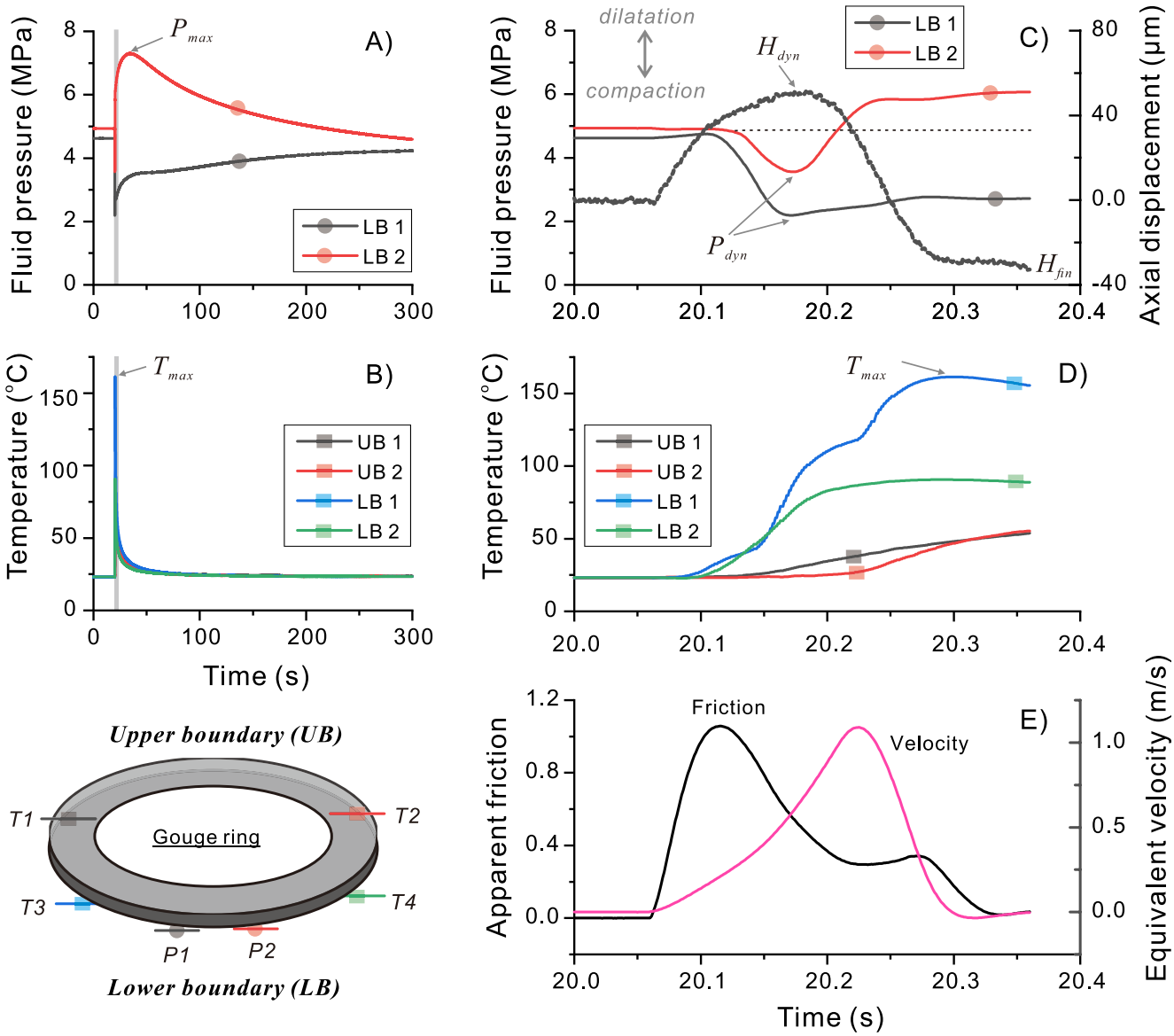

Figure 4. Typical results obtained in a high-velocity slip pulse experiment (run 2427) performed on a simulated Basal Zechstein gouge sample under σ_n^e of 15.5 MPa. All samples tested showed qualitatively similar behavior. (a and b) Evolution of fluid pressures (P) and temperatures (T) versus experiment time; (c and d) enlargement of the P–T changes and the axial displacement during the high-velocity slip pulse; and (e) apparent friction coefficient, $\mu_a = \tau/(\sigma_n - P_i)$, and equivalent velocity profiles during the slip pulse.

different values as the slip decelerated. As slip ceased and time proceeded, the two pressure signals continued to increase for another 20–30 s. Finally, the higher one decreased, and the two P-signals started to converge to 4.3 MPa (roughly the initial level, Figure 4a). Such heterogeneity in the fluid pressures, as reflected by the two transducers, hinders us from correcting the apparent friction of the slip pulse as we did for the pre-slip stage (cf., Figure 3). As indicated above, this was due to a poor (different) hydraulic connection between the transducer and the gouge layer. Differences also exists in the T-measurements made on either side of the gouge layer, especially on the side indicative of localized slip. This can, to some extent, reflect the uneven distribution of shear traction over the slip surface. Several factors may lead to such T-heterogeneity such as the exact positions of welding points of the thermocouples, spatial heterogeneity in the normal stress, and variations in fluid-related characteristics (e.g., local porosity and fluid pressure).

Figure 4e shows the evolution of apparent friction versus displacement, as well as the velocity profile. During the high-velocity slip pulse, shear stress increased abruptly upon initial acceleration. A distinct peak occurred within the first 0.01–0.03 m of slip, followed by significant slip weakening toward a minimum (dynamic) friction

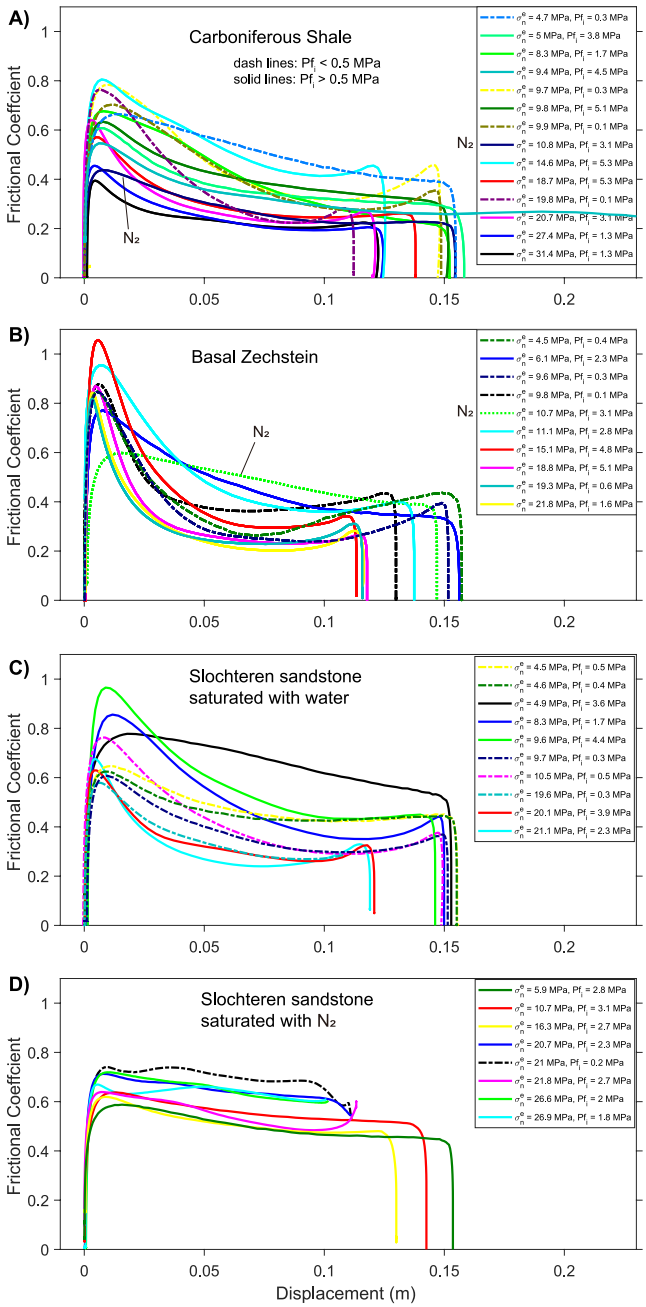

Figure 5. Compiled results showing the evolution of apparent friction coefficient, $\mu_a = \tau/(\sigma_n - P_i)$, with load-point displacement. (a) Carboniferous siltstone/shale, water-saturated except where labeled N_2; (b) basal Zechstein, water-saturated except where labeled N_2; and (c and d) Slochteren sandstone with water and nitrogen as the pore fluid, respectively.

attained at displacements of 7–14 cm, where the velocity reached the maximum. As velocity decreased, friction generally increased until displacement halted at the end of the experiment (motor stopped), at which point the shear stress rapidly fell to zero. The shape of the slip-weakening trajectory as a function of displacement varies between the experiments, showing a roughly logarithmic weakening in some cases (e.g., Figure 4e) versus more linear behavior in others. Similar results on the evolution of friction were obtained in the experiments performed on all gouges and at all σ_n^e employed (Figure 5), although the velocity profile achieved varied slightly in terms of peak velocity and total displacement, depending on the effective normal stress applied and the frictional strength of the material.

The above example of slip pulse data corresponds to an experiment performed at high initial fluid pressure and with the principal slip zone localized at the LB of the gouge layer. A few experiments (e.g., run 2497) showed *T* data indicating localization at the UB and only small (<0.4 MPa), delayed *P* fluctuations (Figure S3 in Supporting Information S1 and cf., Hunfeld et al., 2021). Others (e.g., run 241) performed at low fluid *P* showed a pressure drop to sub-atmospheric values at an early stage of the pulse (i.e., in accordance with the measured dilatation) and a delayed increase after the slip ceased (Figure S4 in Supporting Information S1). Aside from the *P*–*T* measurements, the general evolution of friction and dilatation with time were similar for the three experiments (Figure 4, Figures S3 and S4 in Supporting Information S1), but quantitative differences exist (see Section 3.3).

3.2. Complete Data Set for Wet and N_2-Saturated Samples: Friction Curves

Figure 5 shows all seismic slip pulse results obtained for the Carboniferous siltstone/shale, Basal Zechstein, and Slochteren sandstone gouges, wet and dry (N_2-saturated). The data are presented in terms of μ_a versus shear displacement during the seismic slip pulse. In general, the evolution of μ_a resembles that shown in Figure 4, reaching peak friction at short displacement (<10 mm), followed by slip weakening to a minimum friction value, usually achieved at the peak velocity, and then by a re-strengthening effect as the slip velocity decreased. A few experiments performed at relatively low σ_n^e (<6.1 MPa) showed continued slip weakening during the entire slip pulse (i.e., without re-strengthening).

Interestingly, experiments performed using low (<0.5 MPa) and high (>0.5 MPa) initial fluid pressures displayed distinct behaviors (the dashed and solid lines in Figure 5, hereafter referred to as the "low-*P*" and "high-*P*" experiments, respectively). Specifically, the low-*P* experiments showed consistently high peak friction, with different rates of frictional slip weakening at different applied normal stresses. By contrast, in high-*P* experiments, the peak friction decreased significantly with normal stress, and frictional slip weakening rates were similar, as manifested by nearly parallel curves (Figure 5).

By comparison with the water-saturated (wet) runs, the experiments employing N_2 as the pore fluid (referred to as "dry" experiments) showed generally lower peak strength and much less slip weakening (Figures 5a–5d), resulting in higher dynamic friction levels beyond the peak, regardless of σ_n^e or *P* (Figure 5d).

3.3. Earthquake Source Parameters Determined From the High-*P* Experiments

The post-peak slip-weakening part of the curves obtained in our wet and dry experiments is broadly similar to previous results for fault gouges, as described in the empirical equations proposed by Mizoguchi et al. (2007) or

Di Toro et al. (2011). These equations are equivalent to one another and only differ in how they define the characteristic displacement for slip weakening (D_w). In our study, D_w is defined, following Mizoguchi et al. (2007), as the post-peak slip distance over which shear stress (or apparent friction) drops to a conceptual 5% of the initial peak value in the framework of an empirical fit of the function

$$\mu_a = \mu_{ss} + (\mu_{pk} - \mu_{ss})e^{[\ln 0.05(d-d_{pk})/D_w]} \quad (1)$$

to each slip weakening curve. Here, μ_a is the dynamic friction, and d_{pk} is the displacement measured up to the peak friction (μ_{pk}). The value of μ_{pk} corresponds to the peak friction, while nominal steady-state friction μ_{ss} and D_w were determined using the linear least squares fitting method. In runs where re-strengthening occurs during the deceleration phase, we fit Equation 1 to the data obtained between the peak and the minimum friction (defined as $\mu_{\min}$). In other runs where friction continues to decrease during the entire slip pulse, we fit the above equation to the entire post-peak friction curve. Note that a nominal steady state was not achieved in either case, so that μ_{ss} obtained from the fitting method is always lower than the minimum friction reached in the experiments. Based on the fitting curve, the fracture energy (G_c) corresponding to each high-velocity pulse experiment was determined by taking the integral of Equation 1 from μ_{pk} over D_w. For all the experiments, normalized friction curves based on the fitting parameters are shown in Figure S5 in Supporting Information S1, except for the dry Slochteren sandstone samples which do not display much weakening. In this representation, all curves (i.e., from both high- and low-P experiments) merge to form a single band of slip weakening behavior between the peak friction and the minimum friction, with a characteristic (normalized) slip distance that is equal to e^{-1}.

The corresponding best-fitting parameters for wet gouge samples tested at $P > 0.5$ MPa (i.e., high-P experiments) are shown in Figure 6, plotted versus the initial effective normal stress. Results from the low-P (<0.5 MPa) and dry (N_2) experiments are excluded as these data obscure the trends. This may be because different microphysical processes were operating in the experiments, especially in the early stages. Generally, for the three materials tested, the conceptual steady-state friction and characteristic slip weakening distance (μ_{ss} and D_w), fitted using Equation 1, show a clear decrease with increasing σ_n^e, consistent with previous studies obtained for natural fault gouges (e.g., Mizoguchi et al., 2007; Yao et al., 2013). Specifically, Carboniferous siltstone/shale gouges showed the lowest μ_{pk} and μ_{ss} values. The peak friction shows a decrease with increasing σ_n^e for the Carboniferous siltstone/shale and sandstone gouge samples, whereas high values ranging from 0.8 to 1.05 was maintained for Basal Zechstein samples at all σ_n^e. The fracture energy, G_c, shows no clear dependence on σ_n^e for any of the sample materials tested wet at $P > 0.5$ MPa, but, in all cases, falls in a narrow range between around 0.10 and 0.35 MJ/m^2.

The fitting parameters obtained using the above approach provide useful input parameters for numerical modeling of seismic rupture behavior of both natural and induced seismicity (Buijze et al., 2019; Tinti et al., 2004). However, in the present data set obtained at high water P and high σ_n^e, the values recovered for μ_{pk}, μ_{ss}, and D_w all depend on σ_n^e (Figure 6), and are clearly interdependent to some extent, which makes practical application to numerical simulations potentially difficult.

In an alternative approach, we characterized the shear stress versus displacement data obtained in our wet experiments conducted at $P > 0.5$ MPa from the perspective of stress drop and slip weakening rate, inspired by the observation that the friction-displacement curves are roughly parallel to each other (e.g., Figure 5a). Accordingly, without any fitting procedure, we obtained the dynamic shear stress drop ($\Delta\tau$), the maximum weakening rate ($W_{\max}$), and the average weakening rate (W_{ave}), from the shear stress-displacement curves. Here $\Delta\tau$ is the difference between peak and minimum shear stresses, $W_{\max}$ is the maximum slope in the slip weakening curve (in units of Pa/m), and W_{ave} is the average stress drop rate (Pa/m) measured from peak to minimum stress over the corresponding displacement (see definitions in the insets of Figure 7).

Figure 7 plots our data for the above three parameters as a function of initial effective normal stress for all gouge materials tested. For comparison, we only include data obtained using high-pressure water as pore fluid (cf., Figure 6). As indicated by the dashed lines in Figure 7, all three parameters ($\Delta\tau$, $W_{\max}$, and W_{ave}) display a more or less linear dependence on effective normal stress. Interestingly, their sensitivities to effective normal stress (i.e., the slopes in Figures 7a–7c) roughly double from Carboniferous siltstone/shale to Slochteren sandstone gouge and again from Slochteren sandstone to Basal Zechstein gouge.

To further characterize the shape of the slip weakening curves obtained for samples tested using high-pressure water as pore fluid ($P > 0.5$ MPa), we plot normalized frictional curves in Figure 8. Here, the friction coefficient is normalized by the total (maximum) friction drop displayed by each sample, that is, $\mu^* = (\mu - \mu_{\min})/(\mu_{pk} - \mu_{\min})$,

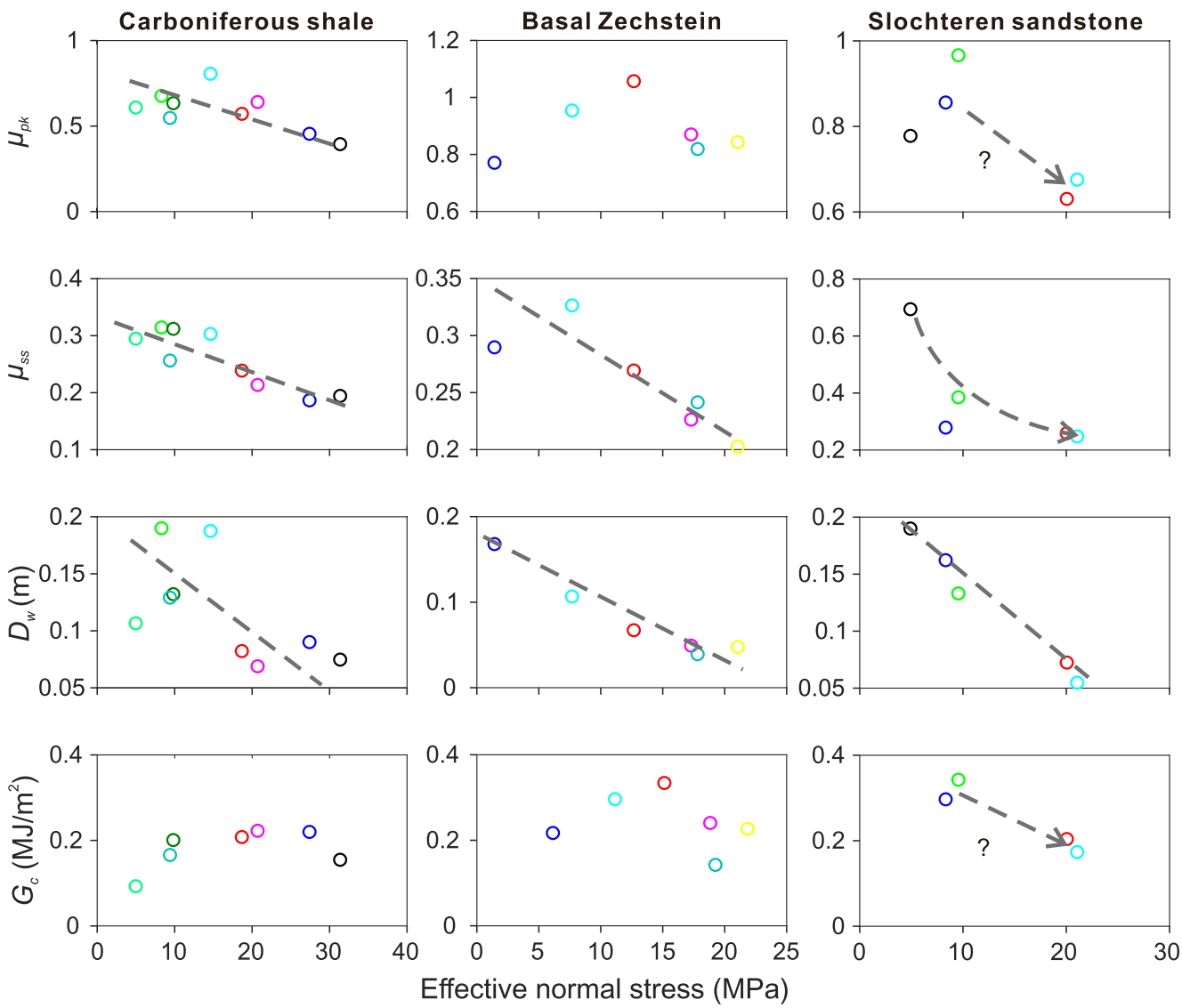

Figure 6. Comparison of friction parameters (i.e., peak friction, μ_{pk}, nominal steady-state friction, μ_{ss}, characteristic slip weakening distance, D_w, and fracture energy, G_c), obtained for the three different gouge materials tested using high initial fluid pressure ($P > 0.5$ MPa) and water as the pore fluid. Parameter values are plotted as a function of initial σ_n^e. The dashed lines highlighting the trends are estimated by eye.

and the slip distance is normalized with respect to the total imposed displacement, that is, $d^* = (d - d_{pk})/d_{\max}$, where $d_{\max}$ is the total displacement. For the three materials tested, the normalized slip weakening curves obtained show a steady, similar decrease in slope with displacement. The shape of the curves can be captured by a standard power-law decay equation of the form,

$$\mu^* = (1 + d^*)^n. \quad (2)$$

The results show that the exponents n fall in the ranges −3 to −6, −5 to −7, and −4 to −6, for the Carboniferous siltstone/shale, the Basal Zechstein, and the Slochteren sandstone gouge materials, respectively (Figure 8). For the individual experiment, a power-law decay function fits most of the slip weakening trajectory well. For each material, the power exponents show a tendency to decrease with σ_n^e (Figure 8).

3.4. Dilatation, and Local Temperature and Fluid Pressure Data

Following the approach illustrated in Figure 4, we determined five key parameters from the dilatation, fluid pressure, and temperature measurements made during each experiment. Specifically, we determined the maximum

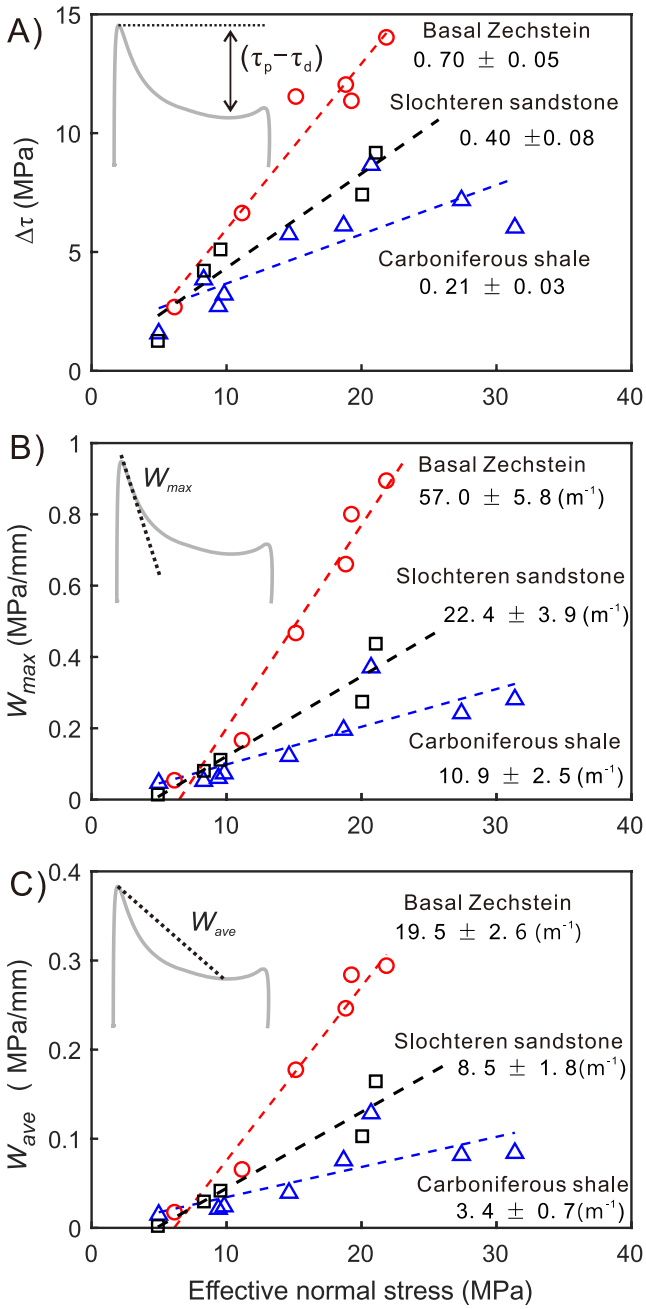

Figure 7. (a) Dynamic strength drop, (b) maximum, and (c) average weakening rates versus initial effective normal stress determined for all three materials tested in experiments using high-pressure water as the pore fluid (P > 0.5 MPa). The dashed lines are linear least squares fits to the data (with free intercept), with the best-fit slope plus error indicated for each case.

change in axial displacement during the acceleration stage (ΔH_{dyn}) of each run, the final thickness change (ΔH_{fin}, both measured with respect to initial thickness), the fluid pressure change achieved during the acceleration phase (ΔP_{dyn}), the maximum pressure increase that was usually reached after the slip pulse (ΔP_{max}), and the maximum temperature measured during the active slip (T_{max}). Since the two pressure transducers located in the lower piston (Figure 4) may have sensed different pressure changes during seismic slip, we recorded the two separate ΔP_{dyn}-values. From the temperature measurements made in the upper and lower pistons (together with observations made on the deformed samples), the location of the slip boundary was inferred for each run. All the measurement results and associated information are listed in Table 1—for all samples.

Our results for almost all samples tested under different fluid types (N_2 and water) and initial pressure conditions showed the positive thickness increase ΔH_{dyn} (dilatation) during accelerating slip, followed by compaction in the late stages of, or after, the slip pulse. This was not the case for the samples that were pre-sheared at effective normal stresses lower than the applied stress during the seismic slip stage. In these cases, ongoing compaction was observed (Table 1). In most experiments, net compaction ($\Delta H_{fin} > 0$) was observed after the cessation of slip.

For all high-P experiments using water as the fluid medium at $P > 0.5$ MPa, the pore pressure measurements showed a pressure decrease upon imposing seismic slip ($\Delta P_{dyn} < 0$), at least at one of the two transducers, while in the low-P experiments (<0.5 MPa water), such depressurization was minor as sub-atmospheric values were attained (Figure S3 in Supporting Information S1). The amplitude of the pressure changes measured in low- and high-P water experiments was much larger in runs where slip had localized near the LB of the sample than in experiments where slip localized near the upper boundary. In the latter case, changes in fluid pressure were strongly damped by the buffering effect of the gouge layer over its full thickness. For the experiments using N_2 as the fluid medium, the measured pressure changes were subtle during the seismic slip. In this case, the dynamic thickness change (ΔH_{dyn}) showed either dilatation or compaction, without a clear trend, although the absolute values were generally larger than those at "wet" conditions. Conclusively, the fluid depressurization effect was pervasive for almost all the experiments using high-P water as a fluid medium, corresponding to a dilatation at the early stage of the pulse. Qualitatively, the pressure change (ΔP_{dyn}), as shown in Figure 9, shows a negative relation with dilatation (ΔH_{dyn}) but does not correlate with effective normal stress.

For all the experiments performed, the maximum pressure changes (ΔP_{max}) were mostly observed after the slip pulse (e.g., reached in ~20 s, Figure 4, Figures S3 and S4 in Supporting Information S1) and varied significantly from experiment to experiment (from 0.2 to 5.0 MPa). Generally, higher ΔP_{max}-values were observed when the deformation localized on the LB, close to the pressure transducers. The observed time delay suggests the existence of pressure heterogeneity and subsequent equilibration within the gouge layer, either over the thickness or in angular position. Again, the maximum changes in fluid pressure were subtle when N_2 was used as the fluid medium.

The maximum temperatures (T_{max}) measured in all wet experiments (i.e., both low and high P) were generally less than 200°C, with a maximum value of 220°C. By contrast, in the dry (N_2 saturated) experiments, T_{max} was mostly above 300°C, reaching 489°C in run 2552 (Table 1). For all the materials tested, the T_{max}-values reached in the experiment do not show a clear trend with increasing effective normal stress. Given the location of the active thermocouple junctions in our set-up, directly at the piston-gouge interfaces (Figure 2c), T_{max} can be considered

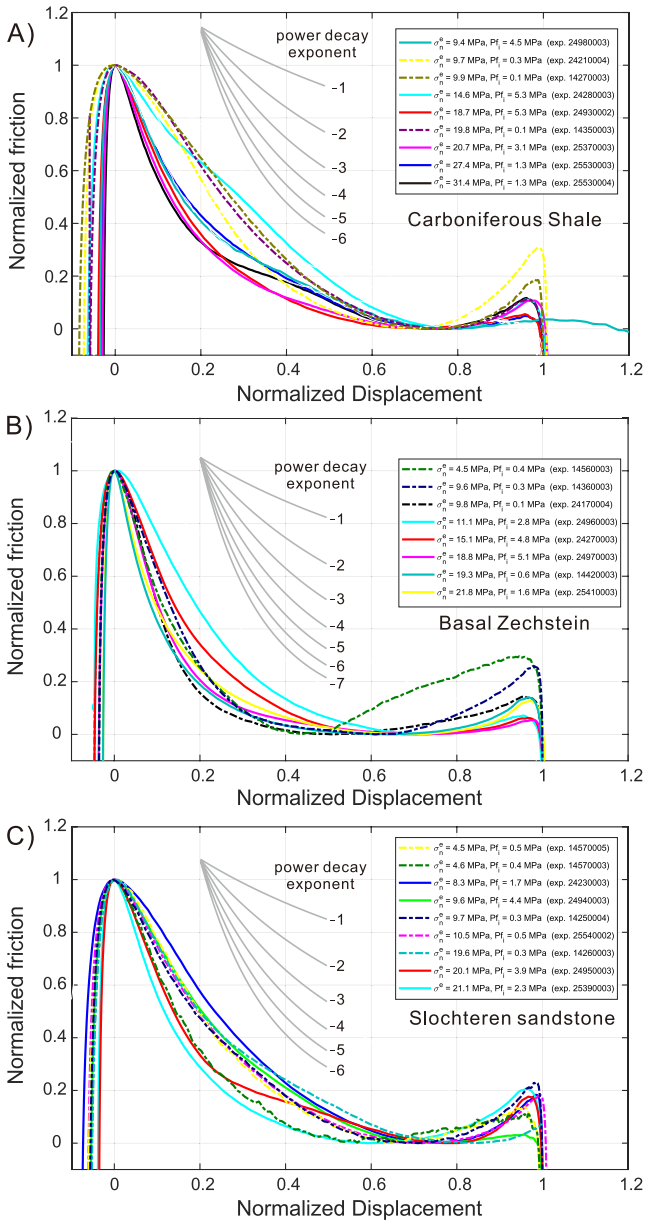

Figure 8. Normalized slip weakening curves obtained for the slip pulse experiments using high-pressure water as the fluid medium. (a, b, and c) are results for the annotated three gouge materials tested. The normalized weakening curves are compared with power-law decay curves with different exponents. Note that the initial position of individual curves is offset for comparison.

as the minimum peak in temperature near the shear band. Microstructures of the samples after the experiments revealed a shear band of 80–150 μm in thickness (Figures 10–11, Figures S6 and S7 in Supporting Information S1). From the theoretical solution for temperature evolution in a shear zone of a fixed thickness (Andrews, 2002; Rice, 2006), the maximum temperature rise at the center of the shear band could be 1.1–1.2 times higher than that at the boundary (assuming a thermal diffusivity of 1e−6 m^2/s for a water-saturated gouge layer).

3.5. Microstructural Observations

Figures 10 and 11 present typical microstructural images of the deformed Carboniferous shale and Slochteren sandstone gouge layers. Both samples were recovered from the experiments using an effective normal stress of ~9.5 MPa and high fluid pressure (P_i) of ~4.5 MPa. In both samples, a localized shear band, with a thickness of ~150 μm, was developed at the lower side of the gouge layer, characterized by strong grain size reduction compared with the rest of the layer (i.e., the bulk layer, see the white dashed lines for their boundaries in Figures 10 and 11a). This, in the combination of the smoother, shinier surfaces developed at the lower boundaries (Figures 10f, 11d and 11e), supports the interpretation of slip localization from the results of the T-measurements. As given in Table 1, during the seismic slip pulse applied in both experiments, higher maximum temperatures were observed at the LB compared with those at the upper boundary. In some samples, shear bands are developed at both boundaries. In this case, we found that on the boundary measuring higher temperatures, the shear band developed appears to be more homogeneous and has finer grain sizes (Figure S6 in Supporting Information S1).

The Carboniferous shale gouge shows a compacted structure in both the shear band and bulk layer (Figure 10b). Interestingly, even thinner, scattered deformation zones were developed in the shear band, with orientation (sub-)parallel to the shear direction, and length extents ranging from a few tens to a few hundreds of micrometers, as indicated by the yellow dashed lines in Figure 10b (hereafter termed "microslip zones"). These scattered microslip zones were recognized from high-magnification images, such as those shown in Figures 10c and 10d (indicated by arrays of yellow arrows). Pores or voids were also irregularly present on both sides of the microslip zones (Figure 10d). Occasionally, "local openings" that connect nearby pores can be seen within the microslip zones (Figure 10e). Similarly, the lower shear band in the sandstone gouge is characterized by relatively high porosity and small grain sizes, specifically where narrow, shear-parallel dilatant microslip zones are also developed (Figure 11c). Unlike the Carboniferous shale gouge, shear-parallel bands are also seen in the bulk layer of the sandstone gouge (see yellow dashed lines, Figure 11b). The Basal Zechstein gouge is well compacted after the experiments at both high- and low-P conditions. Unlike other gouge samples, the microslip zone does not develop, but a large number of "voids" are seen in the shear band, with diameters varying from 0.5 to 10 μm (Figure S6 in Supporting Information S1).

Finally, we note that the microstructures do not show much difference between the samples recovered from the low- and high-P experiments, although, as addressed above, different samples have gone through different (local) fluid pressure paths during the experiments. The only (minor) differences were found in the sandstone samples (cf., Figure 11, Figure S7 in Supporting Information S1). The sandstone gouge sheared in the low-P experiment was more fragile and porous, consisting of a shear band of higher porosity and a bulk layer containing plenty of shear-parallel openings (Figure S7 in Supporting Information S1). Here, we only investigated two samples. To

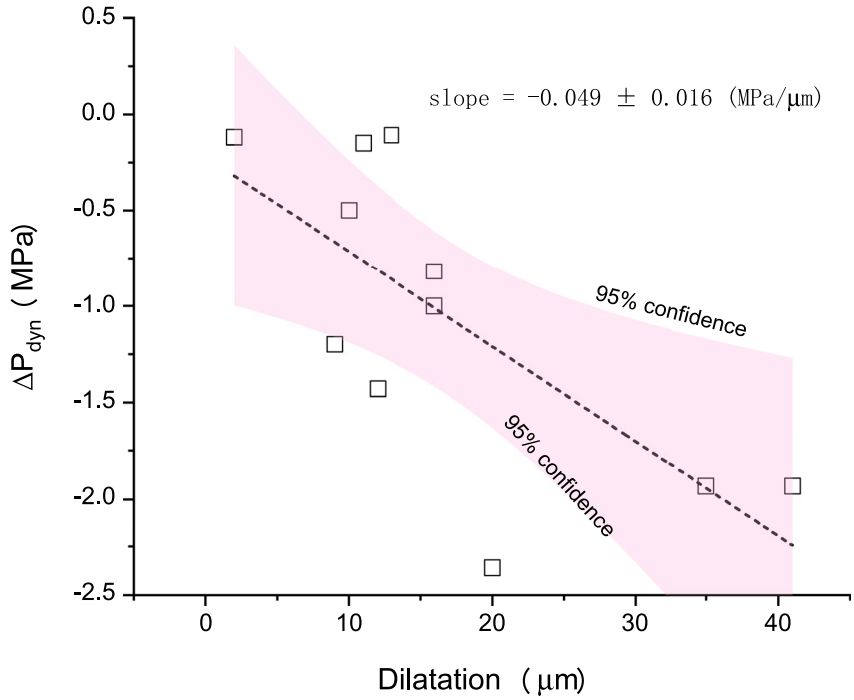

Figure 9. Relation between gouge dilatation and the dynamic pore fluid pressure drop upon imposing the slip pulse. Data are derived from 11 experiments, where (1) the simulated gouges had been pre-sheared at the same applied normal stress as during the slip pulse, (2) slip was inferred to localize shear at the lower boundary, and (3) high-*P* water was used as the fluid medium.

fully assure the difference, microstructural investigation of sheared samples under a wide range of fluid pressures is warranted in the future.

4. Discussion

In the present study, we provide a systematic data set on the dynamic frictional properties of simulated fault gouges prepared from key rock units in the Groningen field by means of high-velocity slip pulse experiments. The experiments were performed under conditions that simulate M3–4 earthquake slip under close to the in-situ conditions of the Groningen gas reservoir (Hunfeld et al., 2021). Relatively high initial fluid pressure (up to 5 MPa) was used, and the highest effective normal stress reached was 31 MPa. The slip acceleration imposed by the HVF machine used in the present study is on average ~9 m/s^2 and up to 32 m/s^2, resulting in a seismic slip rate (1–1.5 m/s) being reached after ~0.14 s and a total displacement of ~0.15 m. These conditions are made to mimic not only induced M3–4 earthquake events in Groningen but also natural seismic events of similar magnitude (cf., the kinematic modeling results given by Buijze, van den Bogert, et al. (2017) and Wentinck (2018)). Here, we briefly summarize our key observations on the mechanical behavior, before proceeding to evaluate the controlling mechanisms and implications for induced seismicity in the Groningen gas field.

4.1. Wet Versus Dry Slip Pulse Behavior

One of the key observations of the present study is that all simulated fault gouge materials tested wet (either high or low pressure) showed rapid slip weakening during short-displacement seismic slip (~0.15 m) representative of an earthquake of small magnitude, while the same materials saturated with N_2, do not weaken much, even though much higher temperatures were reached due to frictional heating.

Unlike a seismic slip experiment reproducing large natural seismic events, where, regardless of fault rock lithology, a nearly complete loss of frictional strength can be achieved given a sufficiently long displacement, under wet or dry conditions (Di Toro et al., 2011), the present short-displacement, wet-tested faults weakened only to a certain level and then re-strengthened as slip decelerated. The typical absolute drop in friction coefficient varied from 0.2 to 0.5, depending on gouge lithology and effective normal stress applied. Significantly, many of our

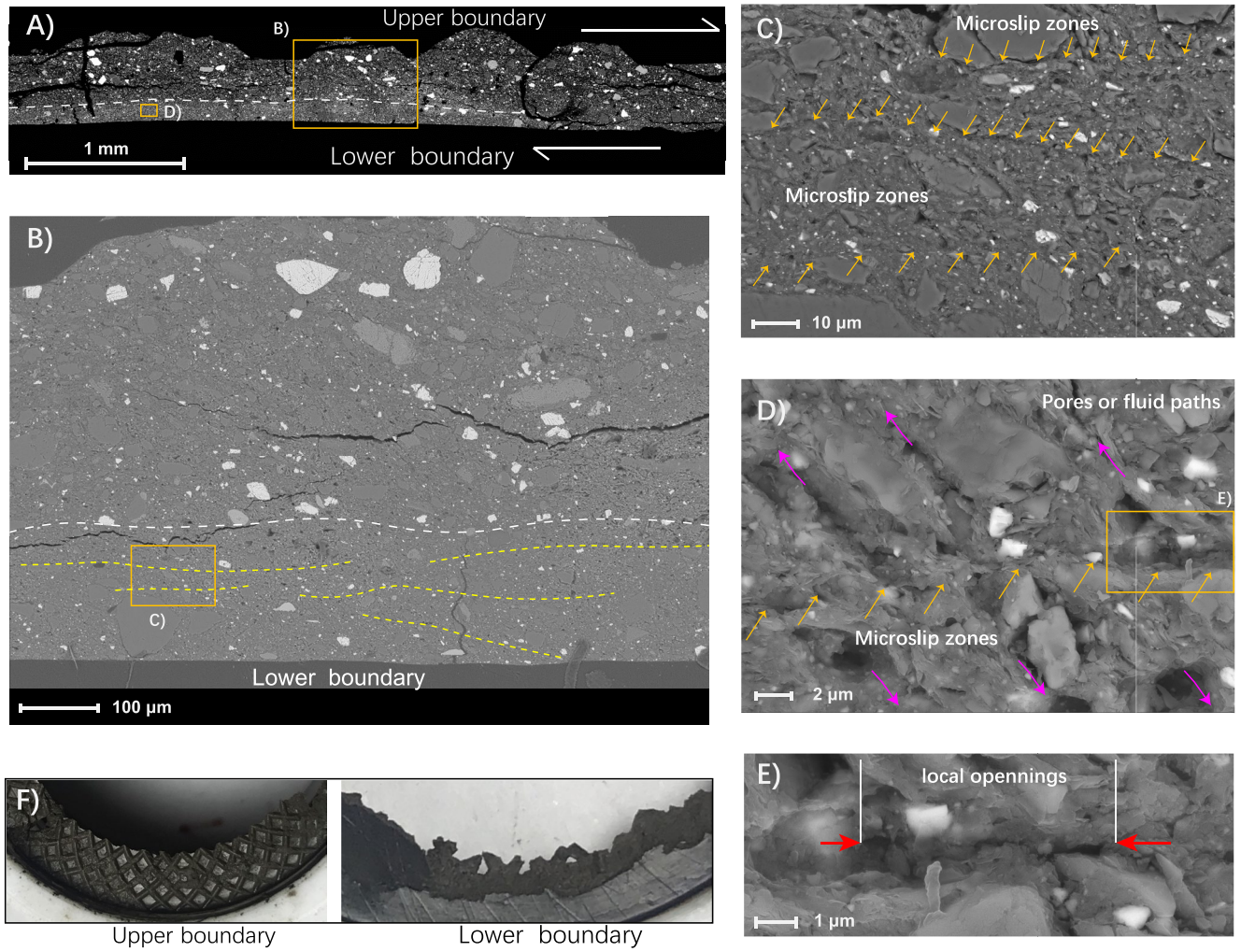

Figure 10. Microstructure of a sectioned Carboniferous gouge sample after the high-speed slip pulse experiment (run 2498, $\sigma_e = 9.4$ MPa and $P_i =$ of 4.5 MPa). (a) Mosaic image of a 5 mm-long gouge segment, showing wavy vs. straight boundaries at the upper and lower sides. The lower side has a fine-grained continuous band with a boundary indicated by the white dashed line. (b) Enlargement of the gouge layer, consisting of a weakly-deformed bulk layer and the lower boundary shear band. (c–e) More localized, scattered "microslip zones" developed in the shear band indicated by arrays of yellow arrows (see the definition in the main text). Panels (a–e) are all backscatter images. (f) Photomicrographs of the retrieved gouge layer taken from the upper and lower sides.

wet experiments tested under high initial pore pressure ($P_i > 0.5$ MPa) showed a decrease in peak friction with increasing effective normal stress, especially for simulated Carboniferous siltstone/shale gouge. This differs from previous findings for wet Groningen gouges where the pore water pressure was drained to atmospheric pressure (Hunfeld et al., 2021). In the following, we examine the weakening mechanism(s) operating at high water pressures that are more representative of the natural fault conditions than addressed previously (Hunfeld et al., 2021; Oohashi et al., 2015).

4.2. Mechanisms for Weakening in the High-*P* Experiment

Several weakening mechanisms have been proposed to explain the dynamic weakening of a wet fault at seismic slip rates, such as compaction-driven pore fluid pressurization (Oohashi et al., 2015), thermal pore fluid pressurization (Badt et al., 2020; Faulkner et al., 2011; Hunfeld et al., 2021; Togo et al., 2011), thermochemical pressurization (Brantut et al., 2010), bulk melting (Tsutsumi & Shimamoto, 1997), silica gel lubrication (Di Toro et al., 2006), thermally activated super-plasticity (De Paola et al., 2015), pore water phase transitions from the liquid to the gaseous or supercritical state (Chen et al., 2017; Ferri et al., 2010), and flash heating (B. P. Proctor et al., 2014; Yao et al., 2018). The absence of dramatic weakening in the N_2 experiments suggests that none of the

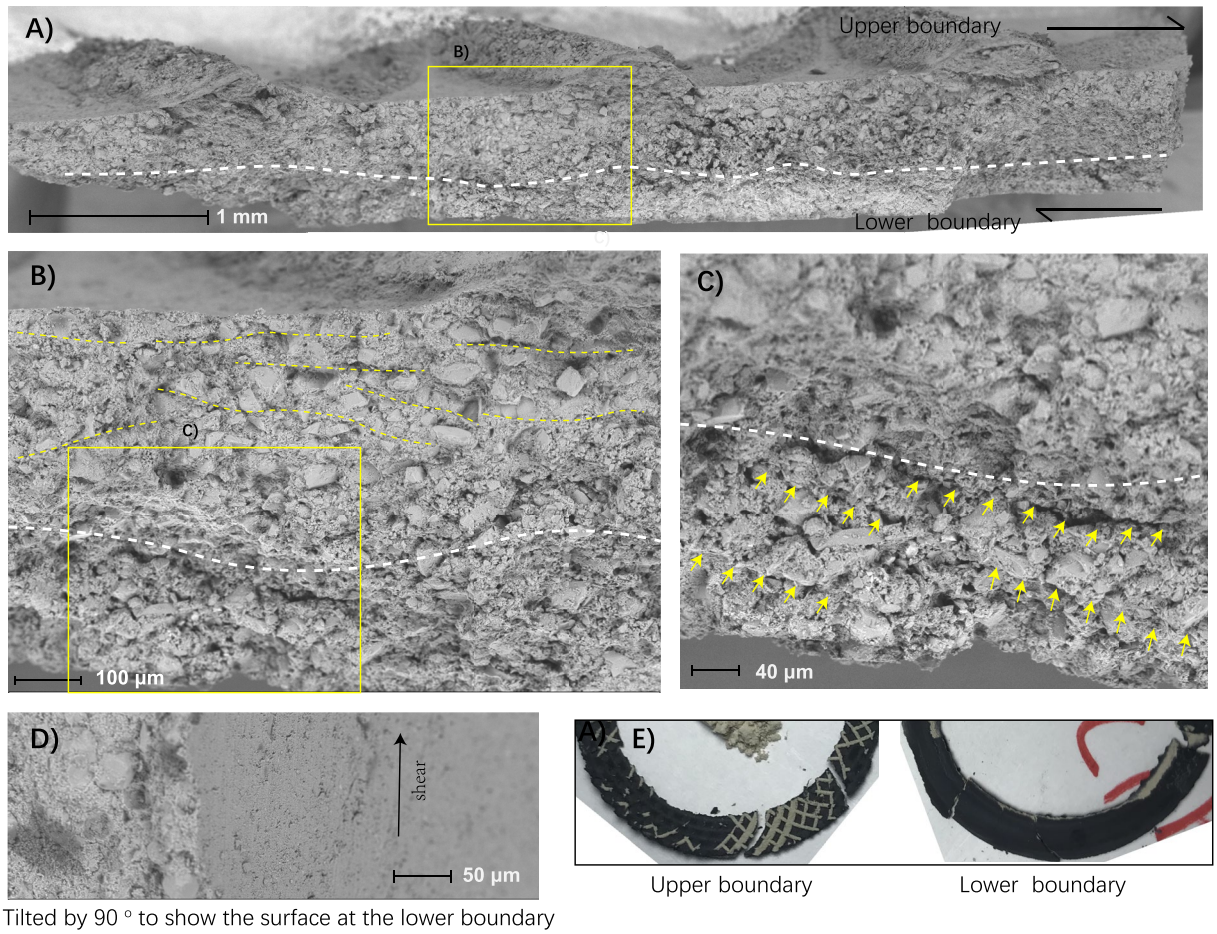

Figure 11. Microstructure of a sample fragment of the Slochteren sandstone gouge retrieved after the high-speed slip pulse experiment (run 2494, $\sigma_e = 9.6$ MPa and $P_i =$ of 4.4 MPa). (a) Mosaic image of a 6 mm-long gouge segment. The lower side has a continuous fine-grained band with a boundary indicated by the white dashed line. (b) Enlargement of the gouge layer, consisting of a weakly-deformed bulk layer and the shear band. (c) Zoom of the shear band, characterized by relatively high porosity, the presence of abundant voids, and shear-parallel "microslip zones" indicated by the arrays of yellow arrows. (d) Image of the tiled thin section by 90°, showing the smooth surface of the gouge layer at the lower boundary. Panels (a–d) are all backscatter images. (e) Photos of the retrieved gouge segments, showing the upper and lower surfaces.

condition(s) to stimulate the abovementioned weakening mechanisms was met. Meanwhile, our observations in the high-P water experiments seem incompatible with all of these mechanisms as well.

First, after pre-shearing the gouge at a low slip rate, dilatation was observed when first subjected to a seismic slip pulse. This excludes compaction-related pressurization as the dynamic weakening mechanism (Faulkner et al., 2018). Second, our pore fluid pressure measurements, made close to the active shear band, revealed a pressure decrease during the acceleration stage of the slip pulse, almost without exception, and this behavior is notable in experiments employing high initial fluid pressure (see Table 1). Such fluid pressure decrease accompanying dilatation has also been observed in recent seismic slip experiments using either bare rock surfaces or fault gouges (Aretusini et al., 2021; Brantut, 2020; B. Proctor et al., 2020). This eliminates bulk (gouge-wide) thermal pressurization as the weakening mechanism. Third, our temperature measurements demonstrated increases of less than 220°C in our wet experiments (under either high or low initial fluid pressure), far below the temperature needed for bulk melting, decomposition, or superplastic flow of the minerals contained in the gouge materials. For the most vulnerable mineral, illite (which is up to 21 wt% in the Carboniferous shale), the dehydration reaction is too slow to reach a considerable fraction of reacted material (<0.2%), given the short duration of our experiment and a reaction rate of ~0.25 min^{-1} (Mikhail & Guindy, 1971). Moreover, a re-strengthening phase was observed in most wet experiments (Figure 5), and it occurred almost in phase with the deceleration (Figure 4, Figures S3 and S4 in Supporting Information S1). This again helps exclude some of the mechanisms such as bulk melting and decomposition, since the temperature still went up for some time during the deceleration (Figure 4).

Fourth, the use of three different rock types excludes composition-related weakening mechanisms such as silica gel lubrication or decarbonation. Finally, in our wet experiments performed using high initial fluid pressures, the possibility of the phase transition from liquid pore water to vapor occurring, and overpressuring the fault gouges tested, is minimal (e.g., Chen et al., 2017).

A remaining candidate mechanism is flash heating which is commonly reported as a plausible mechanism for dynamic weakening at (sub-)seismic slip rates, notably for sliding of rock-on-rock surfaces (Beeler et al., 2008; Goldsby & Tullis, 2011). High "flash" temperatures, caused by sliding of highly stressed asperities, lead to thermal weakening of localized asperities, for example, via dehydration, decarbonation, or melting, and thus to a reduction in the shear stress supported. Spagnuolo et al. (2015) proposed that the rapid weakening observed in their short-displacement slip pulse experiments on room-dry blocks of Carrara marble is due to plastic deformation at the asperity scale, where fast-moving dislocations produce an abrupt flash temperature rise leading to the formation of amorphous carbon which further lubricates the fault. However, to what extent flash asperity heating is effective in gouges with differing and mixed mineral compositions, particularly in the presence of water, remains speculative. This is (a) because the shear velocity is distributed over many grain contacts in the localized zone of the gouge layer, and (b) because of the "quenching" effect of the pore fluid (Chen et al., 2017; Yao et al., 2016).

As a first-order approximation, frictional heating at asperities can be estimated following the classical flash heating model (B. P. Proctor et al., 2014; Rice, 2006). For simplicity, we first assume a dry model, from which the flash temperature calculated can reasonably represent the upper bound of the temperature in a wet material. As given in Text S1 in Supporting Information S1, for an average weakening velocity of 0.25 m/s (e.g., Figure 4e) and using our best estimate of the parameters needed, the characteristic weakening temperature (T_w) falls in the range of 212°C–449°C. Given such low T_w-values, we can conclude that classical flash heating produces insufficient temperature increase to explain the weakening observed in our wet experiments, because in these experiments the real temperature increase would be lower than calculated for dry material (i.e., due to the thermal capacity of the pore fluid). Another reason for excluding flash heating as the weakening mechanism in the wet experiment is that our dry experiments, even with higher bulk temperatures being measured (Table 1), do not show dramatic weakening. If flash heating played an important role in the wet experiments, it would have caused strong weakening in the dry experiments as well.

4.2.1. Present Weakening Mechanism—Flash or Local Pressurization?

The fact that our water-saturated fault gouges slip-weaken substantially while dry ones do not, means that water must be involved in the underlying mechanism. Based on this observation and the concept of flash heating, we propose fluid pressurization at the asperity scale, hereafter referred to as "flash pressurization," may be the mechanism that causes the high degree of slip weakening seen in our wet high-P experiments (Figure 12). Conceptually, we see this mechanism as a combination of flash heating and thermal pressurization, occurring on the grain contact (asperity) scale, as opposed to thermal pressurization at the shear band or gouge-wide scales. This interpretation is supported by the microstructures of the shear bands, which show an abundance of "voids" in various sizes (i.e., from submicron to a few 10s of micrometers, Figure 11, Figure S6 in Supporting Information S1 for the Slochteren sandstone and Basal Zechstein gouges, respectively), indicating the presence of locally overpressurized fluid during deformation.

An alternative explanation would be thermal pressurization at the scale of exceedingly localized slip bands (i.e., scattered fine-scale slip bands within the shear band) whose margins are sealed sufficiently to allow thermal pressurization but not readily detected at the points of T and P measurement. This process is supported by the presence of narrow, more localized deformation zones that extend from a few tens to a few hundreds of micrometers within the shear band ("microslip zones," Figures 10 and 11, in the Carboniferous and Slochteren sandstone gouges, respectively). At this stage, we cannot distinguish between "flash pressurization" and thermal pressurization of these extremely-localized microslip zones (or "local pressurization"). At some point, they become the same thing (i.e., the same macroscopic consequences)–it is just a question of how many grains the microslip zone contains in its thickness (cf., Figure 12a).

4.2.2. A Qualitative Model for Flash/Local Pressurization

To illustrate the flash pressurization hypothesis, we construct a simplified conceptual model. As shown in Figure 12a, we assume that, during a seismic slip pulse, deformation is dominated by granular flow in the

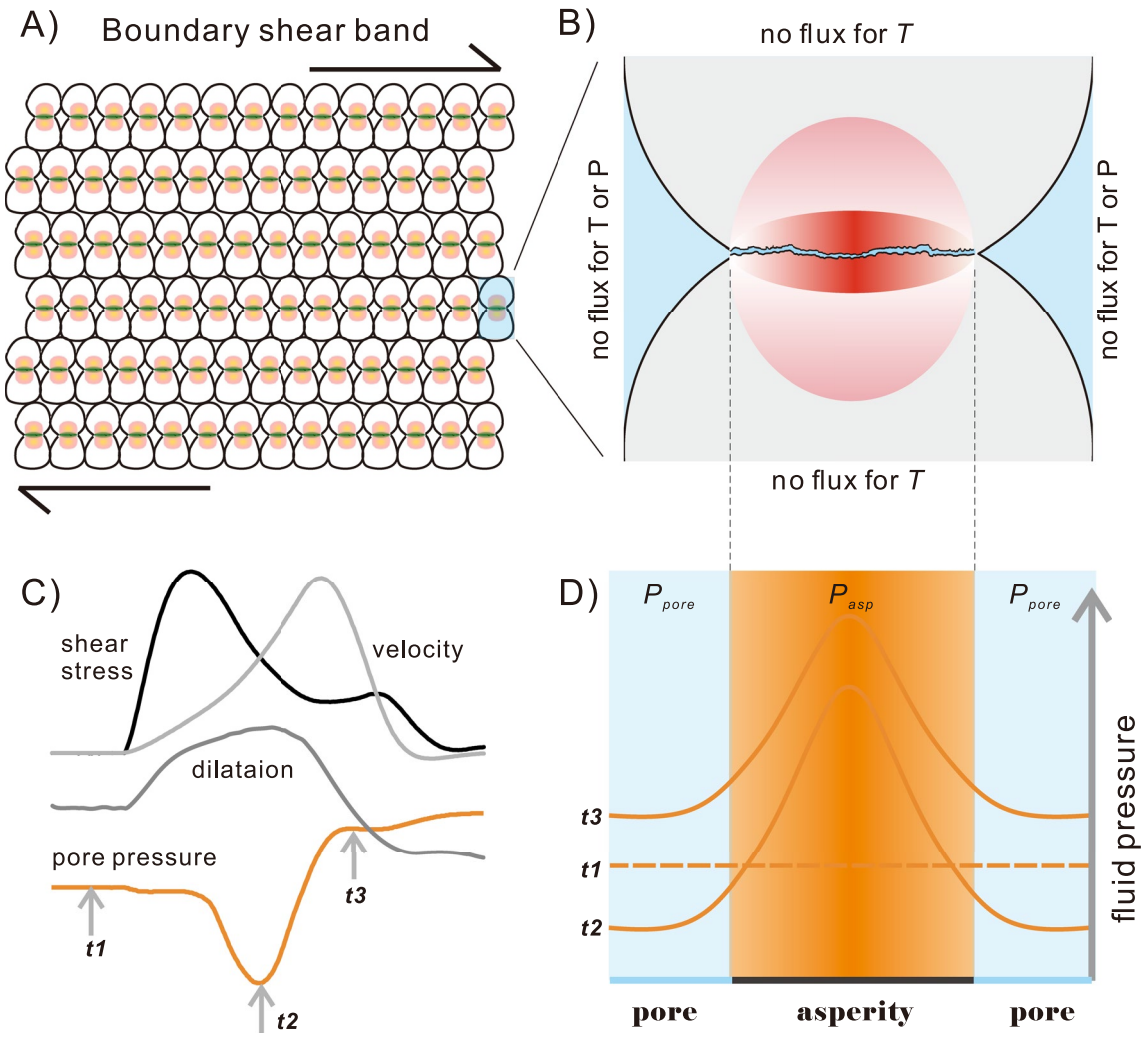

Figure 12. Schematics of a hypothetical mechanism (termed "flash pressurization") proposed here to account for dynamic weakening during the present seismic slip pulse experiments on samples saturated with water at elevated pore fluid pressure (cf., Oohashi et al., 2015; Yao et al., 2018). (a) Idealized grain pack within a shear band developed near the upper or lower boundary of a simulated gouge layer. (b) An unit cell representing the grain-pack structure, with flash heating occurring at the sliding grain contact (or asperity) during high velocity (seismic) slip. (c) Typical data obtained in a seismic slip pulse experiment in the present study (compare with Figure 4), including shear stress, dilatation, and fluid pressure evolution (with time) measured immediately adjacent to the shear band. (d) Profile of fluid pressure across the unit cell at different stages of the slip pulse.

localized shear band observed near the lower sample-piston interface in most experiments and formed by cataclasis in the pre-shear stage. A unit cell of deformation within the shear band consists of two half grains in contact (Figure 12b) and sliding over each other at an average slip rate $\tilde{V} = V/N_a$, where V is the imposed slip rate, and N_a is the number of sliding grain "layers" in the shear band. As in the classical flash heating model, frictional heat will be generated at the asperities bearing high local stresses. However, in wet samples, water will be present in the pore space and on the grain surface, that is, within asperity interfaces. Assuming the asperity-sliding process occurs in all neighboring cells, then, on the short time scale investigated, a unit cell can be taken to experience symmetrical (zero flux) boundary conditions for both thermal and fluid diffusion. We emphasize again that similar boundary conditions can also be satisfied by the "local pressurization" model, given that the microslip zones are wide and/or bounded by impermeable margins. Based on this configuration, let us now explore the thermo-hydro-mechanical coupling processes within a unit cell, as constrained by observations from a typical experiment.

As the seismic slip starts, the shear band will dilate as grains ride over each other, causing a decrease in the pore pressure (i.e., pressure within the light blue area, Figure 12b). Meanwhile, as individual grains (the asperity) slide over each other, heat will be generated due to flash heating at a source rate similar to that in the dry case,

$$Q_a = \tau_c \times \tilde{V}. \quad (3)$$

Here, τ_c is the (local) shear stress at the grain contact (in the unit of Pa), $\tilde{V}$, as indicated above, is the grain boundary sliding rate (in the unit of m/s), and Q_a is the resultant heat generation rate (in the unit of Wm^{-2}). The time scale for this process is assumed to be the contact lifetime t_a,

$$t_a = D_a/\tilde{V}, \quad (4)$$

where D_a is the diameter of the asperity. Note that while higher $\tilde{V}$ increases Q_a, it decreases t_a. The total amount of frictional heat released at an asperity during the lifetime would always be $E_a = Q_a t_a = \tau_c D_a$ (Figure 12b). Since the thickness of the grain boundaries is likely to be very thin (order of nm, Chen & Spiers, 2016), the pressure of water layers trapped in the contacting boundary may not be in equilibrium with the water pressure in the pore space during rapid intergranular sliding in the time scale t_a. Therefore, in the early stage of a slip pulse, the fluid pressure within the pore space (P_{pore}) could be lower than the initial value that has been lowered by dilatation, while the pressure of water film within the contact area or asperity (P_{asp}) can still increase due to flash heating (Figures 12c and 12d), which reduces the apparent friction of the asperity and causes weakening. This scenario offers a possible explanation for the seemingly opposite observations during the early stage of the slip pulse made on wet samples tested at elevated water pressure, namely, dilatation and pore fluid depressurization, versus low peak friction and fast weakening (cf., the low-P experiments). As slip continues, the pressurized water at the asperity, together with the heat it carries, would (re)enter the pore space, and the flash heat is also transferred through diffusion. The combination of heat and fluid transfers causes temperature rise and pressurization in the pore water, namely, thermal pressurization in the conventional sense (Figure 12d). Depending on the local fluid drainage condition, this would cause a re-distribution of pore pressure and thus effective normal stress acting on the fault surface, which offers a compelling explanation for the heterogeneous temperature rise and pressure change between different sensors during the seismic slip pulse (Figure 4, Figures S3 and S4 in Supporting Information S1). Finally, as slip decelerates, the heat production rate at the asperities or micro-slip zones decreases immediately (Equation 3), causing the decrease in the local pressures, and therefore, a re-strengthening phase.

Note that for the dry (N_2) experiments, the above processes may also occur at the local scales (i.e., at either the grain contact or microslip zone scale), but the associated de/pressurization effects during de/acceleration would be greatly reduced due to high compressibility of N_2. This may explain the absence of dramatic weakening and re-strengthening in the dry experiments.

4.2.3. Comparison With Previous Models for Wet Weakening

Oohashi et al. (2015) have reported drastic slip weakening of smectite-rich gouges at slip rates of 1.3 mm/s and under water-saturated conditions. They interpreted that the dynamic weakening at these intermediate velocities could be attributed to pore pressure increases caused by both shear-enhanced compaction and microscopic vaporization of pore water on/around asperities. Since in our experiments the critical distance for the initial dynamic weakening is much smaller (~0.02 mm vs. >0.1 m), the critical velocity (V_w) was much higher (~0.25 m/s vs. ~1.3 mm/s), and compaction-caused pressurization is negligible, the underlying mechanisms responsible for the incipient weakening in the two studies are not exactly the same. In most of our experiments, we used high initial fluid pressures (3–5 MPa), which could minimize the occurrence of water vaporization due to higher boiling temperatures corresponding to these fluid pressures (i.e., in both macroscopic and microscopic scales). Moreover, the pre-shear imposed in the present study could reduce the grain size and thus the asperity size for generating flash heating (i.e., 200 nm–1 μm), while Oohashi et al. (2015) adopted a 10 μm asperity size for their calculation.

Yao et al. (2018) have also observed dramatic weakening of two fault gouges at sub-seismic slip rates ($V \geq 0.04$ and ≥0.4 m/s) and wet conditions, similar to that observed in the present study. They proposed a similar process in their experiments (i.e., the boiling of water at asperity scales) but suggested that pressurization by water vaporization only plays a secondary role while vaporization of water layers may weaken asperity contacts directly (somewhat similar to the thermal softening process on asperities due to thermal decomposition). Similar processes involving the phase transition of water on the asperity scale have been proposed to operate during spontaneous stick slips in low-velocity friction experiments (Acosta et al., 2018). Rempe et al. (2020) also performed gouge-shear experiments in the presence of pressurized fluid (up to 10.5 MPa), and the assembly used enabled a good drainage of fluid from the gouge to the porous spacer (at least at the initiation of sliding at high velocity). Different from the present observation, the transient dilatation was only observed at ~0.5 m of displacement,

indicating that bulk fluid pressurization was unlikely responsible for the observed weakening. Likewise, bulk fluid pressurization was ruled out as an efficient weakening mechanism for cohesive carbonate rocks, based on the modest dilatation and expansion of pore fluids during the deformation (Violay et al., 2014).

In all, the flash or local fluid pressurization proposed in the present paper is put forward here as a conceptual model that may offer an explanation for our experimental observations on wet samples under high fluid pressures. To test if this model is feasible, numerical modeling and perhaps tribological experiments are needed at the asperity contact and/or grain/pore scale.

4.3. Implications for Induced Earthquakes

The present study focuses on small induced earthquakes occurring under reservoir conditions, specifically in the Groningen gas field, though this can also be viewed as a more general example of small magnitude earthquake slip. The key message emerging from our results is that a water-saturated fault or fault segment, regardless of gouge type, does weaken substantially during slip at the rates and displacements corresponding to earthquakes of magnitude 3–4 (i.e., slip ~10 cm, Buijze, van den Bogert, et al., 2017; Wentinck, 2018). Figure 13 summarizes the fault strength and dynamic weakening rate of gouges derived from the key stratigraphic units in the Groningen gas field. The most rapid weakening is observed in the experiments on Basal Zechstein anhydrite-carbonate gouge (representative of the caprock), which show the highest peak strength, the largest dynamic stress drops, and the highest weakening rates. This behavior suggests that faults incorporating gouge material derived from the anhydrite-carbonate caprock at the reservoir top are the most energetic during an earthquake rupture event. Interestingly, the anhydrite-carbonate caprock has also been identified to be the most sensitive to earthquake nucleation from the rate-and-state frictional properties point of view (Hunfeld et al., 2017, 2019). The 10 Boer claystone, based on the previous studies by Hunfeld et al. (2021), shows low peak strength and low dynamic friction. Considering that this is a relatively thin unit (Figure 1), this formation poses the least resistance to rupture propagation, and therefore an earthquake rupture would not be readily arrested within this layer. Neither is it likely to be prone to rupture nucleation (Hunfeld et al., 2021). By contrast, both the Slochteren sandstone reservoir rock and the Carboniferous siltstone/shale substrate show substantial dynamic weakening (friction drop from 0.65 to 0.3 and from 0.4 to 0.2, respectively, at $\sigma_n^e \sim 20$ MPa). This behavior implies that faults cutting the entire reservoir system (including the Basal Zechstein caprock but also the Carboniferous basement) can slip weaken following reactivation, potentially leading to rapid slip and seismogenesis. All these results, coupled with the stress changes generated around faults due to reservoir depletion and compaction (Buijze et al., 2019; Jansen et al., 2019), are generally consistent with the location/depth distribution of the earthquake hypocenters (e.g., Dost et al., 2017, 2020), which shows that induced events occur over the full extent of the reservoir system with a slightly elevated number of occurrences toward the top of the reservoir.

Independently of gouge lithology, our study reveals that a "dry" or gas-filled fault gouge does not weaken as much as a water-saturated fault material during short-displacement slip events at seismic rates. In the context of the Groningen field, fault segments within the gas-filled interval of the Slochteren sandstone reservoir would not be as dry as in the present N_2 charged experiments and are more likely to be partially wet. To assess the effects of partial water/gas saturation on slip weakening during seismic slip pulses with dm displacement, further experiments may be warranted in the future, though we anticipate that connate water will be sufficient to produce the flash pressurization or local thermal pressurization effect that may control the slip weakening process.

Moreover, most of our wet experiments showed a re-strengthening phase as slip decelerated, especially in the tests performed at high effective normal stress (>10 MPa). A recent study by Violay et al. (2019) has explored the deceleration phase of seismic slip on cohesive faults under varied normal stress and fluid conditions. Our results of re-strengthening are generally consistent with their observation in experiments using Carrara marble. As in our study, these authors also reported enhanced re-strengthening in the presence of water compared with that under room-humidity or vacuum condition. As seen in one of the control experiments in which we doubled the shear displacement, our results further showed that re-strengthening is favored by larger displacement (Figure 5a). When applied to nature, our results suggest that a coseismic re-strengthening phase would preferably occur during larger earthquakes (i.e., at greater depth and with larger displacement). The presence or absence of re-strengthening can also be expected to impact many aspects of the earthquake cycle, including the slip rate evolution during faulting, the pattern of rupture propagation (crack- or pulse-like), the release of seismic waves, the energy budget, as well as post-seismic fault healing and repeat time (Sone & Shimamoto, 2009; Violay

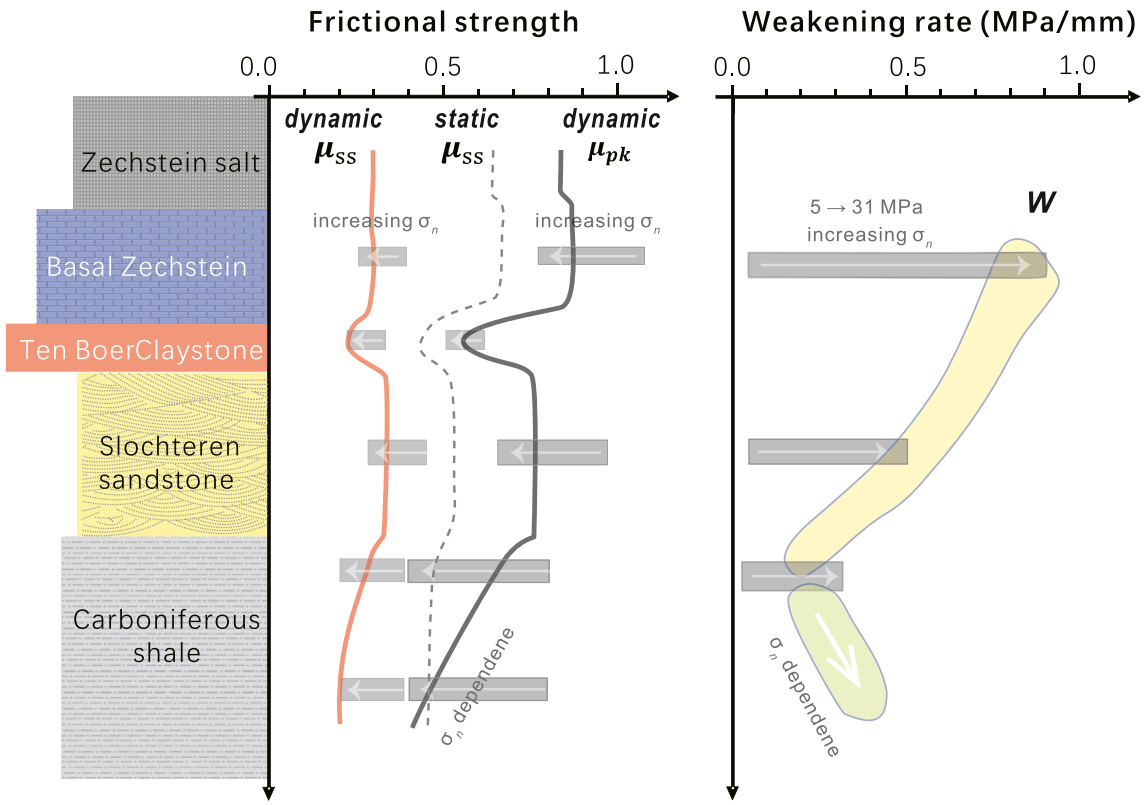

Figure 13. Compilation of Groningen fault strength and dynamic weakening rate data. The stratigraphy of the Groningen gas reservoir (reservoir depth ~3 km, thickness of the Slochteren sandstone layer 150–250 m) and over/underlying units is indicated, along with the corresponding peak and nominal steady-state apparent friction coefficients obtained in the present experiments at 5–31 MPa effective normal stress (denoted respectively as dynamic μ_{pk} and dynamic μ_{ss}), as well as the quasi-static steady-state values characteristic of earthquake nucleation at ~1 μm/s (denoted here as static μ_{ss}) obtained at 40 MPa effective normal stress by Hunfeld et al. (2017). For the Zechstein salt layer, the dynamic steady-state friction is taken from the seismic slip experiment on room-dry halite at 5 MPa normal stress (dynamic $\mu_{ss} = 0.3$, Buijze, Niemeijer, et al., 2017), while the peak and quasi-static steady-state friction was taken from the low-velocity friction experiments on pure halite sheared at room-humidity and 18 MPa normal stress ($\mu_{pk} = 0.83$, and static $\mu_{ss} = 0.64$, Hirauchi et al., 2020).

et al., 2019). To fully understand these effects, systematic experiments varying shear displacement, deceleration rates and fluid conditions are warranted.

A crucial concern regarding the possibility of an earthquake larger than M4 occurring in Groningen lies in the rupture behavior of the underlying rocks, which potentially carry tectonic stress (Figure 1). In the Groningen gas field, the Carboniferous siltstone/shales underlie the reservoir. As addressed above, gouges prepared from this material show relatively low (peak) frictional strength (0.4–0.5) at effective normal stresses of 20–31 MPa. The decrease in measured peak and residual friction with increasing normal stress (Figures 5 and 6) suggests that the increase in shear strength with increasing depth will be less than expected for constant frictional strength. Generally, the Carboniferous siltstone/shale possesses relatively low shear resistance to a downward propagating rupture (Figure 13). However, our study also revealed that the Carboniferous siltstones/shales show the lowest slip-weakening rates. For the dynamic rupture process, this implies relatively low energy release rates, suggesting a relatively sluggish rupture process in the Carboniferous substrate below the Groningen reservoir. Whether or not a rupture can propagate downward from the reservoir interval into the Carboniferous shale/siltstone, where residual tectonic stresses may be present, and how such ruptures will behave in the Carboniferous, requires the use of our data on peak friction, steady-state (or dynamic) friction, slip weakening distance (D_w) and slip weakening rate (W), in appropriate rupture models that include all necessary geomechanical constraints (including the background stresses) to compute the evolving shear stress at rupture tips.

Generally, the present study provides a revised data set on dynamic frictional properties under near in-situ conditions of the Groningen reservoir (revised and improved with respect to the preliminary data presented by Hunfeld et al. (2021)), suitable as input for numerical modeling studies directed at assessing likely rupture sizes and

earthquake magnitudes. Wentinck (2018) showed that a dynamic friction drop from 0.6 to 0.2–0.3 is required to explain slip patch size and stress drop inferred from ground motions and seismic data for the largest induced events that have occurred in the Groningen field to date. These values match well with the friction drop observed in the present experiments. Dynamic modeling of induced earthquakes in Groningen typically assumes a linear slip-weakening model for individual faults, featuring a uniform fault-wide friction drop from 0.6 to values in the range 0.2–0.5, to facilitate earthquake generation (Buijze, van den Bogert, et al., 2017; Buijze et al., 2019). However, there has been little physical basis to underpin the choice of dynamic friction values and slip weakening distances for the various lithologies involved. Here, we independently confirm this range of values and have shown that dynamic slip weakening behavior (during acceleration) can be captured by an exponential and a power-law decay function. Since a nominal steady state was not achieved in the present experiments due to short displacement, the three parameters (μ_{pk}, μ_{ss}, and D_w) obtained by fitting the exponential form to the friction-displacement curves are strongly interrelated. Here, we propose that a power-law function, which contains two independent parameters (μ_{pk} and the decay exponent n), offer a suitable input for dynamic rupture simulations of small-magnitude earthquakes. Implementing our results and the variation in gouge strength and slip-weakening behavior seen between the different stratigraphic units in future modeling studies should help elucidate the mechanisms of earthquake propagation and arrest, as well as improve our understanding of the observed depth, frequency, and magnitude distribution of induced events in the Groningen field and help place constraints on future earthquake magnitudes and hazard—during continued gas production and after production ceases.

5. Conclusions

We performed seismic slip experiments on simulated fault gouges prepared from borehole samples of the key lithologies in the Groningen gas field. The central aim was to quantify the evolution of friction with slip, for slip trajectories that are representative of induced earthquakes such as those occurring in the Groningen field. We employed the rotary-shear, HVF apparatus installed at the Geological Institute of the China Earthquake Administration in Beijing, for which we developed a new ring-shear assembly consisting of a pressure vessel designed to confine the gouge samples and pore fluid. This new design was implemented to remove uncertainties in data obtained in our previous work (Hunfeld et al., 2021), which were associated with imperfect confinement (extrusion) of clay-rich gouge samples. In these experiments, a controlled, short displacement (13–16 cm), high-velocity slip pulse (up to ~1 m/s) was imposed on pre-sheared gouges under effective normal stresses (σ_e) in the range 5.0–31 MPa, initial fluid pressures (P_i) up to 5 MPa using either water or dry N_2 as pore fluid at initially ambient temperature conditions. In addition to reaching high normal stresses (the highest to date), pressurized water was used as pore fluid, which differs from many of the previous studies that used wet gouges (e.g., Hunfeld et al., 2021; Oohashi et al., 2015; Ujiie & Tsutsumi, 2010). Moreover, the new setup allows for the P–T measurements in near-direct contact with the active slip surface. The main findings are summarized as follows:

1. In general, the individual friction curves obtained in the wet experiments showed a sharp weakening as slip accelerated to a seismic rate (0.2–0.3 m/s). In most experiments, a minimum (dynamic) friction was reached at the peak slip rate, consistent with the observation made in our previous study (Hunfeld et al., 2021). Using a wider range of effective normal stress and initially pressurized pore water, we found that dynamic weakening is largest for the Basal Zechstein caprock, with the highest peak and largest friction drop. Gouges derived from the Carboniferous siltstone/shale substrate show the lowest peak strength and less weakening. The Slochteren sandstone reservoir gouges showed an intermediate behavior. In contrast, the experiments using N_2 as fluid did not show much weakening in all the experiments performed.
2. The frictional behavior of the wet experiments strongly depends on the initial fluid pressure. As observed in many previous studies, in the low-P experiments, the frictional curves showed a sharp weakening from nearly constant peak friction, with weakening slopes that strongly depend on effective normal stress. In the high-P experiments, the peak friction also showed a normal stress dependence with the friction-displacement curves running more or less parallel for different effective normal stresses. From this starting point, we found that the slip weakening curves can be normalized using a power-law decay function, with exponents decreasing from −4 to −6 with increasing effective normal stress (from 5 to 31 MPa).
3. Quantitatively, the frictional parameters derived from the frictional curves of the wet, high-P experiments, that is, the peak friction, dynamic friction, characteristic slip distance, friction drop, and slip weakening rate, show a normal stress dependence. The fracture energy showed little or no dependence on normal stress in any of the materials tested.

4. Temperature measurements at both pistons revealed the position of slip localization within the gouge layer during the slip pulse experiments, which was supported by the post-deformation microstructures. On the basis of new measurements made close to the actively slipping zone, we found that thermal pressurization of the pore fluid is not responsible for the weakening observed in all materials, simply because a decrease in pore pressure was always observed at the early stages of the slip pulse, accompanied by dilatation. This first-time observation more or less eliminates all the candidate weakening mechanisms proposed in the literature, including frictional melting, flash heating, and bulk vaporization. Incorporating the representative microstructures, we propose that flash pressurization at the asperities or thermal pressurization of the extremely localized "microslip zones" (i.e., both in the submicron–micron scale) within the localized shear band (i.e., ~100 μm), can account for most of the observations. This remains to be more rigorously tested.
5. The dynamic weakening data and slip-weakening trajectories obtained in the present experiments provide much-needed experimental constraints for dynamic rupture simulations in the Groningen gas field. These are free of artifacts that may be present in our earlier data for gouges prepared from the Carboniferous siltstones/shales below the Groningen reservoir (Hunfeld et al., 2021), which is a formation of special interest regarding the possibility of downward rupture propagation from the reservoir interval. Our results show that the Carboniferous basement exhibits the lowest slip weakening rate of all materials tested (1/4 of that for the Basal Zechstein), suggesting a relatively slow rupture process on faults in this formation. The precise implications of this will emerge from future applications of our data in dynamic rupture models for the field. Beyond Groningen, the results can also generally underpin dynamic modeling of seismic rupture in hydrocarbon and geothermal fields with lithologies of similar composition and accordingly contribute to improving seismic hazard analysis.

Data Availability Statement

The raw and smoothed experimental data in the present study are freely available online: https://doi.org/10.4121/20179856.

Acknowledgments
This research was funded by the Basic Scientific Funding of Chinese National Nonprofit Institutes (IGCEA2101) during J. Chen's work on the project in the Institute of Geology, China Earthquake Administration in Beijing, and also by the Nederlandse Aardolie Maatschappij (NAM) B.V. (Contract UI49294, Amendments 3 and 4). The authors thank Dr. Huihui Weng and Prof. Jean-Paul Ampuero for their suggestion of applying different fitting protocols to the slip-weakening data, Dr. Lu Yao, Dr. Xi Ma, and Bowen Yu for their assistance in conducting the experiments and microstructural analyses. The authors thank two anonymous reviewers and the Editor for their careful and constructive comments.

References

Acosta, M., Passelegue, F. X., Schubnel, A., & Violay, M. (2018). Dynamic weakening during earthquakes controlled by fluid thermodynamics. *Nature Communications*, *9*(1), 3074. https://doi.org/10.1038/s41467-018-05603-9

Andrews, D. J. (2002). A fault constitutive relation accounting for thermal pressurization of pore fluid. *Journal of Geophysical Research*, *107*(B12), 2363. https://doi.org/10.1029/2002JB001942

Aretusini, S., Meneghini, F., Spagnuolo, E., Harbord, C. W., & Di Toro, G. (2021). Fluid pressurisation and earthquake propagation in the Hikurangi subduction zone. *Nature Communications*, *12*(1), 2481. https://doi.org/10.1038/s41467-021-22805-w

Badt, N. Z., Tullis, T. E., Hirth, G., & Goldsby, D. L. (2020). Thermal pressurization weakening in laboratory experiments. *Journal of Geophysical Research: Solid Earth*, *125*(5), e2019JB018872. https://doi.org/10.1029/2019jb018872

Beeler, N. M., Tullis, T. E., & Goldsby, D. L. (2008). Constitutive relationships and physical basis of fault strength due to flash heating. *Journal of Geophysical Research*, *113*(B1), B01401. https://doi.org/10.1029/2007jb004988

Boneh, Y., & Reches, Z. (2018). Geotribology—Friction, wear, and lubrication of faults. *Tectonophysics*, *733*, 171–181. https://doi.org/10.1016/j.tecto.2017.11.022

Brantut, N. (2020). Dilatancy-induced fluid pressure drop during dynamic rupture: Direct experimental evidence and consequences for earthquake dynamics. *Earth and Planetary Science Letters*, *538*, 116179. https://doi.org/10.1016/j.epsl.2020.116179

Brantut, N., Schubnel, A., Corvisier, J., & Sarout, J. (2010). Thermochemical pressurization of faults during coseismic slip. *Journal of Geophysical Research*, *115*(B5), B05314. https://doi.org/10.1029/2009JB006533

Buijze, L., Niemeijer, A. R., Han, R., Shimamoto, T., & Spiers, C. J. (2017). Friction properties and deformation mechanisms of halite(-mica) gouges from low to high sliding velocities. *Earth and Planetary Science Letters*, *458*, 107–119. https://doi.org/10.1016/j.epsl.2016.09.059

Buijze, L., van den Bogert, P. A. J., Wassing, B. B. T., & Orlic, B. (2019). Nucleation and arrest of dynamic rupture induced by reservoir depletion. *Journal of Geophysical Research: Solid Earth*, *124*(4), 3620–3645. https://doi.org/10.1029/2018JB016941

Buijze, L., van den Bogert, P. A. J., Wassing, B. B. T., Orlic, B., & ten Veen, J. (2017). Fault reactivation mechanisms and dynamic rupture modeling of depletion-induced seismic events in a Rotliegend gas reservoir. *Netherlands Journal of Geosciences*, *96*(05), s131–s148. https://doi.org/10.1017/njg.2017.27

Chen, J., Niemeijer, A., Yao, L., & Ma, S. (2017). Water vaporization promotes coseismic fluid pressurization and buffers temperature rise. *Geophysical Research Letters*, *44*(5), 2177–2185. https://doi.org/10.1002/2016GL071932

Chen, J., & Spiers, C. J. (2016). Rate and state frictional and healing behavior of carbonate fault gouge explained using microphysical model. *Journal of Geophysical Research: Solid Earth*, *121*(12), 8642–8665. https://doi.org/10.1002/2016JB013470

De Paola, N., Holdsworth, R. E., Viti, C., Collettini, C., & Bullock, R. (2015). Can grain size sensitive flow lubricate faults during the initial stages of earthquake propagation? *Earth and Planetary Science Letters*, *431*, 48–58. https://doi.org/10.1016/j.epsl.2015.09.002

Di Toro, G., Han, R., Hirose, T., De Paola, N., Nielsen, S., Mizoguchi, K., et al. (2011). Fault lubrication during earthquakes. *Nature*, *471*(7339), 493–499. https://doi.org/10.1038/nature09838

Di Toro, G., Hirose, T., Nielsen, S., Pennacchioni, G., & Shimamoto, T. (2006). Natural and experimental evidence of melt lubrication of faults during earthquakes. *Science*, *311*(5761), 647–649. https://doi.org/10.1126/science.1121012

Dost, B., Ruigrok, E., & Spetzler, J. (2017). Development of seismicity and probabilistic hazard assessment for the Groningen gas field. *Netherlands Journal of Geosciences*, *96*(5), 235–245. https://doi.org/10.1017/njg.2017.20

Dost, B., van Stiphout, A., Kühn, D., Kortekaas, M., Ruigrok, E., & Heimann, S. (2020). Probabilistic moment tensor inversion for Hydrocarbon-Induced seismicity in the Groningen gas field, The Netherlands, Part 2: Application. *Bulletin of the Seismological Society of America*, *110*(5), 2112–2123. https://doi.org/10.1785/0120200076

Ellsworth, W. L. (2013). Injection-induced earthquakes. *Science*, *341*(6142), 1–8. https://doi.org/10.1126/science.1225942

Faulkner, D. R., Mitchell, T. M., Behnsen, J., Hirose, T., & Shimamoto, T. (2011). Stuck in the mud? Earthquake nucleation and propagation through accretionary forearcs. *Geophysical Research Letters*, *38*(18), 1–5. https://doi.org/10.1029/2011GL048552

Faulkner, D. R., Sanchez-Roa, C., Boulton, C., & denHartog, S. A. M. (2018). Pore-fluid pressure development in compacting fault gouge in theory, experiments, and nature. *Journal of Geophysical Research: Solid Earth*, *123*(1), 226–241. https://doi.org/10.1002/2017jb015130

Ferri, F., Di Toro, G., Hirose, T., & Shimamoto, T. (2010). Evidence of thermal pressurization in high-velocity friction experiments on smectite-rich gouges. *Terra Nova*, *22*(5), 347–353. https://doi.org/10.1111/j.1365-3121.2010.00955.x

Goldsby, D. L., & Tullis, T. E. (2011). Flash heating leads to low frictional strength of crustal rocks at earthquake slip rates. *Science*, *334*(6053), 216–218. https://doi.org/10.1126/science.1207902

Hanks, T. C., & Bakun, W. H. (2008). M-log*A* observations for recent large earthquakes. *Bulletin of the Seismological Society of America*, *98*(1), 490–494. https://doi.org/10.1785/0120070174

Harbord, C., Brantut, N., Spagnuolo, E., & Di Toro, G. (2021). Fault friction during simulated seismic slip pulses. *Journal of Geophysical Research: Solid Earth*, *126*(8), e2021JB022149. https://doi.org/10.1029/2021JB022149

Hergert, T., Haug, C., Henk, A., & Nüchter, J.-A. (2022). Modelling production-induced dynamic rupture of intra-graben faults and related earthquakes in the North German Basin. *Geomechanics for Energy and the Environment*, *32*, 100339. https://doi.org/10.1016/j.gete.2022.100339

Hirauchi, K., Yoshida, Y., Yabe, Y., & Muto, J. (2020). Slow stick-slip failure in halite gouge caused by brittle-plastic fault heterogeneity. *Geochemistry, Geophysics, Geosystems*, *21*(9), e2020GC009165. https://doi.org/10.1029/2020GC009165

Hunfeld, L. B., Chen, J., Niemeijer, A. R., Ma, S., & Spiers, C. J. (2021). Seismic slip-pulse experiments simulate induced earthquake rupture in the Groningen gas field. *Geophysical Research Letters*, *48*(11), e2021GL092417. https://doi.org/10.1029/2021gl092417

Hunfeld, L. B., Chen, J., Niemeijer, A. R., & Spiers, C. J. (2019). Temperature and gas/brine content affect seismogenic potential of simulated fault gouges derived from Groningen gas field caprock. *Geochemistry, Geophysics, Geosystems*, *20*(6), 2827–2847. https://doi.org/10.1029/2019GC008221

Hunfeld, L. B., Niemeijer, A. R., & Spiers, C. J. (2017). Frictional properties of simulated fault gouges from the seismogenic Groningen gas field under in-situ P-T-chemical conditions. *Journal of Geophysical Research: Solid Earth*, *122*(11), 1–21. https://doi.org/10.1002/2017JB014876

Jansen, J. D., Singhal, P., & Vossepoel, F. (2019). Insights from closed-form expressions for injection- and production-induced stresses in displaced faults. *Journal of Geophysical Research: Solid Earth*, *124*(7), 7193–7212. https://doi.org/10.1029/2019JB017932

Kuo, L.-W., Hung, C.-C., Li, H., Aretusini, S., Chen, J., Di Toro, G., et al. (2022). Frictional properties of the Longmenshan fault belt gouges from WFSD-3 and implications for earthquake rupture propagation. *Journal of Geophysical Research: Solid Earth*, *127*(5), e2022JB024081. https://doi.org/10.1029/2022jb024081

Kuo, L.-W., Wu, W.-J., Kuo, C.-W., Smith, S. A. F., Lin, W.-T., Wu, W.-H., & Huang, Y.-H. (2021). Frictional strength and fluidization of water-saturated kaolinite gouges at seismic slip velocities. *Journal of Structural Geology*, *150*, 104419. https://doi.org/10.1016/j.jsg.2021.104419

Liao, Z., Chang, J. C., & Reches, Z. (2014). Fault strength evolution during high velocity friction experiments with slip-pulse and constant-velocity loading. *Earth and Planetary Science Letters*, *406*, 93–101. https://doi.org/10.1016/j.epsl.2014.09.010

Ma, S., Shimamoto, T., Yao, L., Togo, T., & Kitajima, H. (2014). A rotary-shear low to high-velocity friction apparatus in Beijing to study rock friction at plate to seismic slip rates. *Earthquake Science*, *27*(5), 469–497. https://doi.org/10.1007/s11589-014-0097-5

Mikhail, R. S., & Guindy, N. M. (1971). Rates of low-temperature dehydration of montmorillonite and illite. *Journal of Chemical Technology & Biotechnology*, *21*, 113–116.

Mizoguchi, K., Hirose, T., Shimamoto, T., & Fukuyama, E. (2007). Reconstruction of seismic faulting by high-velocity friction experiments: An example of the 1995 Kobe earthquake. *Geophysical Research Letters*, *34*(1), L01308. https://doi.org/10.1029/2006GL027931

Oohashi, K., Hirose, T., Takahashi, M., & Tanikawa, W. (2015). Dynamic weakening of smectite-bearing faults at intermediate velocities: Implications for subduction zone earthquakes. *Journal of Geophysical Research: Solid Earth*, *120*(3), 1572–1586. https://doi.org/10.1002/2015JB011881

Proctor, B., Lockner, D. A., Kilgore, B. D., Mitchell, T. M., & Beeler, N. M. (2020). Direct evidence for fluid pressure, dilatancy, and compaction affecting slip in isolated faults. *Geophysical Research Letters*, *47*(16), e2019GL086767. https://doi.org/10.1029/2019GL086767

Proctor, B. P., Mitchell, T. M., Hirth, G., Goldsby, D., Zorzi, F., Platt, J. D., & Di Toro, G. (2014). Dynamic weakening of serpentinite gouges and bare surfaces at seismic slip rates. *Journal of Geophysical Research: Solid Earth*, *119*(11), 2014JB011057. https://doi.org/10.1002/2014JB011057

Rempe, M., Di Toro, G., Mitchell, T. M., Smith, S. A. F., Hirose, T., & Renner, J. (2020). Influence of effective stress and pore fluid pressure on fault strength and slip localization in carbonate slip zones. *Journal of Geophysical Research: Solid Earth*, *125*(11), e2020JB019805. https://doi.org/10.1029/2020JB019805

Rice, J. R. (2006). Heating and weakening of faults during earthquake slip. *Journal of Geophysical Research*, *111*(B5), B05311. https://doi.org/10.1029/2005jb004006

Richter, G., Hainzl, S., Dahm, T., & Zöller, G. (2020). Stress-based, statistical modeling of the induced seismicity at the Groningen Gas Field, The Netherlands. *Environmental Earth Sciences*, *79*(11), 252. https://doi.org/10.1007/s12665-020-08941-4

Sone, H., & Shimamoto, T. (2009). Frictional resistance of faults during accelerating and decelerating earthquake slip. *Nature Geoscience*, *2*(10), 705–708. https://doi.org/10.1038/ngeo637

Spagnuolo, E., Plümper, O., Violay, M., Cavallo, A., & Di Toro, G. (2015). Fast-moving dislocations trigger flash weakening in carbonate-bearing faults during earthquakes. *Scientific Reports*, *5*(1), 16112. https://doi.org/10.1038/srep16112

Tinti, E., Bizzarri, A., Piatanesi, A., & Cocco, M. (2004). Estimates of slip weakening distance for different dynamic rupture models. *Geophysical Research Letters*, *31*(2), L02611. https://doi.org/10.1029/2003GL018811

Togo, T., Shimamoto, T., Ma, S., & Hirose, T. (2011). High-velocity frictional behavior of Longmenshan fault gouge from Hongkou outcrop and its implications for dynamic weakening of fault during the 2008 Wenchuan earthquake. *Earthquake Science*, *24*(3), 267–281. https://doi.org/10.1007/s11589-011-0790-6

Tsutsumi, A., & Shimamoto, T. (1997). High-velocity frictional properties of gabbro. *Geophysical Research Letters*, *24*(6), 699–702. https://doi.org/10.1029/97gl00503

Ujiie, K., Tanaka, H., Saito, T., Tsutsumi, A., Mori, J. J., Kameda, J., et al. (2013). Low coseismic shear stress on the Tohoku-Oki megathrust determined from laboratory experiments. *Science*, *342*(6163), 1211–1214. https://doi.org/10.1126/science.1243485

Ujiie, K., & Tsutsumi, A. (2010). High-velocity frictional properties of clay-rich fault gouge in a megasplay fault zone, Nankai subduction zone. *Geophysical Research Letters*, *37*(24), L24310. https://doi.org/10.1029/2010gl046002

Van Eijs, R. M. H. E., Mulders, F. M. M., Nepveu, M., Kenter, C. J., & Scheffers, B. C. (2006). Correlation between hydrocarbon reservoir properties and induced seismicity in The Netherlands. *Engineering Geology*, *84*(3–4), 99–111. https://doi.org/10.1016/j.enggeo.2006.01.002

van Wees, J.-D., Fokker, P. A., Van Thienen-Visser, K., Wassing, B. B. T., Osinga, S., Orlic, B., et al. (2017). Geomechanical models for induced seismicity in The Netherlands: Inferences from simplified analytical, finite element and rupture model approaches. *Netherlands Journal of Geosciences*, *96*(5), 183–202. https://doi.org/10.1017/njg.2017.38

Violay, M., Nielsen, S., Gibert, B., Spagnuolo, E., Cavallo, A., Azais, P., et al. (2014). Effect of water on the frictional behavior of cohesive rocks during earthquakes. *Geology*, *42*(1), 27–30. https://doi.org/10.1130/G34916.1

Violay, M., Passelegue, F., Spagnuolo, E., Di Toro, G., & Cornelio, C. (2019). Effect of water and rock composition on re-strengthening of cohesive faults during the deceleration phase of seismic slip pulses. *Earth and Planetary Science Letters*, *522*, 55–64. https://doi.org/10.1016/j.epsl.2019.06.027

Weng, H., Ampuero, J.-P., & Buijze, L. (2021). Physics-based estimates of the maximum magnitude of induced earthquakes in the Groningen gas field. *EGU General Assembly*, EGU21-6144. https://doi.org/10.5194/egusphere-egu21-6144

Wentinck, H. M. (2018). *Dynamic modelling of large tremors in the Groningen field using extended seismic sources* (Report for NAM). Shell Global Solutions International B.V. Retrieved from https://nam-feitenencijfers.data-app.nl/download/rapport/996f9a6e-9ef0-47e5-872d-fda8de45be8d?open=true

Yao, L., Ma, S., Chen, J., Shimamoto, T., & He, H. (2018). Flash heating and local fluid pressurization lead to rapid weakening in water-saturated fault gouges. *Journal of Geophysical Research: Solid Earth*, *123*(10), 9084–9100. https://doi.org/10.1029/2018JB016132

Yao, L., Ma, S., Niemeijer, A. R., Shimamoto, T., & Platt, J. D. (2016). Is frictional heating needed to cause dramatic weakening of nanoparticle gouge during seismic slip? Insights from friction experiments with variable thermal evolutions. *Geophysical Research Letters*, *43*(13), 6852–6860. https://doi.org/10.1002/2016GL069053

Yao, L., Ma, S., Shimamoto, T., & Togo, T. (2013). Structures and high-velocity frictional properties of the Pingxi fault zone in the Longmenshan fault system, Sichuan, China, activated during the 2008 Wenchuan earthquake. *Tectonophysics*, *599*, 135–156. https://doi.org/10.1016/j.tecto.2013.04.011